

# Non-axisymmetric standard magnetorotational instability in the upcoming DRESHDYN-MRI experiments – linear and nonlinear dynamics

Ashish Mishra\*

*Helmholtz-Zentrum Dresden-Rossendorf, Bautzner Landstr. 400, D-01328 Dresden, Germany and  
Center for Astronomy and Astrophysics, ER 3-2,  
TU Berlin, Hardenbergstr. 36, 10623 Berlin, Germany*

George Mamatsashvili

*Helmholtz-Zentrum Dresden-Rossendorf, Bautzner Landstr. 400, D-01328 Dresden, Germany and  
Abastumani Astrophysical Observatory, Abastumani 0301, Georgia*

Frank Stefani

*Helmholtz-Zentrum Dresden-Rossendorf, Bautzner Landstr. 400, D-01328 Dresden, Germany*

Magnetorotational instability (MRI) is the most likely mechanism for efficient transport of angular momentum in accretion disks. However, despite numerous efforts, the quest for an unambiguous realization of MRI in experiments is still ongoing. To conclusively identify MRI in the laboratory, a large Taylor-Couette experiment with liquid sodium is under construction at the Helmholtz-Zentrum Dresden-Rossendorf within the DRESHDYN project. Recently, we have determined the optimal range of parameters for the onset of an axisymmetric mode of the standard MRI (SMRI) with a purely axial background magnetic field and analyzed its nonlinear evolution, saturation and scaling properties in the context of the DRESHDYN-MRI experiment. In this sequel paper, we continue SMRI studies and investigate the linear and nonlinear dynamics of non-axisymmetric modes of the instability in a similar magnetized Taylor-Couette setup. For the linear stability analysis, we use  $Pm = \nu/\eta \sim 10^{-5}$  typical of liquid sodium used in the experiment. We show that the achievable magnetic Reynolds  $Rm \sim 40$  and Lundquist  $Lu \sim 10$  numbers in this experiment are large enough for the growth of non-axisymmetric  $|m| = 1$  SMRI modes. For fixed  $\mu$ , the critical  $Rm_c$  for the onset of non-axisymmetric SMRI is about 2-3 time higher than that of axisymmetric SMRI. We follow the evolution of these modes from their exponential growth in the linear regime all over to nonlinear saturation. The structure of the saturated state and its scaling properties with respect to Reynolds number  $Re$  are analyzed, which is relevant and important for the DRESHDYN-MRI experiment having very high Reynolds numbers ( $\sim 10^6$ ). We show that for  $Re \lesssim 10^4$ , the magnetic energy of non-axisymmetric SMRI modes does not saturate and eventually decays due to the modification of the radial shear profile of the mean azimuthal velocity by the nonlinear axisymmetric SMRI, that is, the modified shear profile appears to be stable against non-axisymmetric modes. By contrast, for large  $Re \gtrsim 10^4$ , a sudden rapid growth and saturation of the magnetic energy of non-axisymmetric modes occur, which are radially localized in the turbulent boundary layer near the inner cylinder wall. The saturation amplitude of the non-axisymmetric modes is always a few orders smaller than that of the axisymmetric SMRI mode. We further show that the scaling relations for magnetic energy and torque in the saturated state of SMRI derived for axisymmetric modes in our previous study well carry over to  $|m| \geq 1$  non-axisymmetric ones.

## I. INTRODUCTION

Since the inception of magnetorotational instability (MRI [1]) as the most likely mechanism to transport angular momentum in accretion disks [2], there have been numerous attempts to capture MRI in laboratory [3–7]. The detection of a standard version of MRI (SMRI) with an imposed purely axial magnetic field in a magnetohydrodynamic Taylor-Couette (TC) flow in laboratory is challenging due to the fact that for the onset of SMRI both magnetic Reynolds ( $Rm$ ) and Lundquist ( $Lu$ ) numbers must be high enough  $O(10)$ , which, because of very small magnetic Prandtl numbers ( $Pm \sim 10^{-6} - 10^{-5}$ )

of liquid metals used in the experiments, is very difficult to achieve without destabilizing the flow itself. In spite of great progress over the past two decades on both analytical and numerical sides (see reviews [8, 9]), a clear, definitive and unambiguous identification of SMRI in laboratory still remains a challenge [3–6]. In this respect, recent claims made by the Princeton team on the detection of the axisymmetric and non-axisymmetric modes of MRI [7, 10] are currently being examined. In their experiment, both the axisymmetric and non-axisymmetric modes of the alleged MRI manifest in close proximity to each other and at values of  $Lu$  and  $Rm$  that both are much lower than what global linear stability analysis predicts (see Fig. 8 in Ref. [10]).

By contrast, the helical (HMRI, [11]) and azimuthal (AMRI, [12]) versions of MRI have been characterized and identified conclusively in the liquid metal (GaInSn)

---

\* a.mishra@hzdr.de

experiment PROMISE [13–16]. In spite of this success of the PROMISE experiment, its constructional restriction is not suitable to achieve  $Rm \sim O(10)$  (or  $Re \sim 10^6$ ) required for the onset of SMRI in a magnetized, viscous and resistive TC flow. This motivated the construction of a much bigger TC machine using liquid sodium as a working fluid within the DRES-DYN project [17]. The main advantage of this new, technologically advanced DRES-DYN-MRI machine is its ability to achieve high enough  $Rm \sim 40$  and  $Lu \sim 10$  necessary for SMRI to set on and grow (see Table II in our previous paper [18], see also below). The capabilities of the DRES-DYN-MRI machine are not restricted only to SMRI, but should allow us to experimentally study also Tayler instability [19] and the recently discovered Super-HMRI at positive shear [20]. Previously, we (Mishra et al. [18] hereafter Paper I) conducted a detailed linear analysis of axisymmetric SMRI for the parameter regimes of the upcoming DRES-DYN-MRI experiment. It was shown that SMRI can be detected for all Rayleigh-stable rotation profiles of interest, including the astrophysically important quasi-Keplerian profile, within the ranges of  $Lu$  and  $Rm$  achievable in the DRES-DYN-MRI experiment.

After linear analysis, of immediate interest is nonlinear saturation and evolution of SMRI, which have been extensively investigated since its rediscovery using both astrophysical and laboratory settings [21, 22]. Recent liquid metal experiments of MRI in magnetized TC devices and related numerical simulations have advanced our understanding of the nonlinear saturation and dynamics of SMRI [23–28]. Early work by Liu et al. [23] performed numerical simulations of axisymmetric (with azimuthal wavenumber  $m = 0$ ) SMRI in a TC geometry without endcaps and observed a jet-like outflow at the mid-height of the cylinder, the reconnection layer, and different scalings for normalized perturbation torque at moderate and large magnetic Reynolds numbers, but much lower Reynolds numbers than those found in experiments. Subsequent studies explored the scaling laws for saturation amplitude of energy and angular momentum transport in channel or TC geometry using weakly nonlinear analysis with periodic axial boundary conditions [29–32]. However, these scaling properties turned out to depend on the geometry of the TC setup (thin or wide gap, height of cylinders) in question. Recently, we (Mishra et al. [33], hereafter Paper II) have studied in detail the fully nonlinear evolution and saturation properties of axisymmetric SMRI in a wide-gap TC flow without endcaps and analysed its scaling behaviour over a wide range of  $(Lu, Rm, Re)$  accessible in the DRES-DYN-MRI machine. It was shown that the saturation of SMRI occurs via magnetic reconnection. The dependence of the saturated magnetic energy and torque on Reynolds number was also analyzed and shown to follow a power law scaling  $Re^a$ , where  $-0.6 \leq a \leq -0.5$ , and  $Re^b$ , where  $0.4 \leq b \leq 0.5$ , respectively, at large  $Re \geq 4000$  and all sets of  $(Lu, Rm)$ , so that the exponents always satisfy the relationship  $b - a \approx 1$ .

Relaxing the idealization of infinite cylinders, a number of studies [25–28] focused on the saturation properties and nonlinear dynamics of SMRI in a more realistic setup of finite-height TC flow with top and bottom endcaps primarily in the context of the Princeton MRI experiment. These studies analyzed the dependence of the saturated amplitude on  $Re, Rm$  and  $Lu$  under the influence of insulating or conducting endcaps, and revealed different scalings with  $Pm$  (or  $Re$ ) in these two cases, taking into account the complexity introduced by the presence of Ekman circulations near the top and bottom endcaps.

The main parameters  $Lu, Rm$  and  $Re$  are high enough in the DRES-DYN-MRI experiments (see Table I below) for *non-axisymmetric* ( $m \neq 0$ ) SMRI modes to grow also in parallel with axisymmetric ones, although with smaller growth rate. For clear identification of different modes and the parameter regimes over which each mode can be excited, it is important to study the linear stability of non-axisymmetric modes too. In Papers I and II, we discussed the linear and nonlinear axisymmetric SMRI in the context of DRES-DYN-MRI experiment. Extending this analysis, in this paper, we aim to investigate in detail the dynamics of non-axisymmetric SMRI modes. Although non-axisymmetric SMRI in TC flows has been investigated before both in ideal [34–37] and non-ideal MHD mainly for liquid metals [10, 24, 38, 39], its analysis in the parameter regimes specific to the DRES-DYN-MRI experiments at very small  $Pm \sim 10^{-6} - 10^{-5}$  of liquid sodium and comparison with axisymmetric SMRI mode is still lacking. Motivated by this, in the present paper, we first investigate the linear regime of non-axisymmetric SMRI and then its nonlinear development and saturation, including evolution of magnetic energy and torque, and scaling properties in the saturated state as a function of different system parameters.

The paper is organised as follows. The setup of the problem and the basic equations are described in Sec. II. The formulation of the linear stability problem is given in Sec. III where also discussed are the main results for non-axisymmetric SMRI and the comparison of the growth rates of axisymmetric and non-axisymmetric SMRI modes. Nonlinear evolution and saturation properties of the non-axisymmetric modes are discussed in Sec. IV. A summary and conclusions are presented in Sec. V.

## II. PHYSICAL MODE AND MAIN EQUATIONS

As in papers I and II, we consider a cylindrical TC setup – a basis for the DRES-DYN-MRI experiment, which contains liquid sodium, an incompressible conducting fluid, in the cylindrical coordinate system  $(r, \phi, z)$  (Fig I). In this setup, the inner and outer cylinders with radii  $r_{in}$  and  $r_{out}$  rotate, respectively with angular velocities  $\Omega_{in}$  and  $\Omega_{out}$ . In the DRES-DYN-MRI machine, the ratio of the inner and outer cylinder radii is fixed to  $r_{in}/r_{out} = 0.5$  and the aspect ratio  $L_z/r_{in} = 10$  is

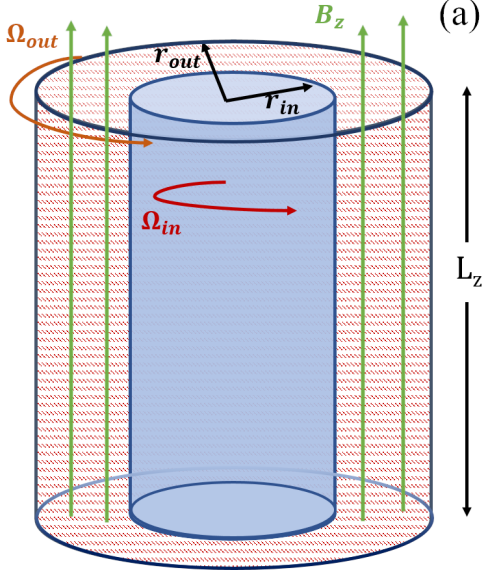


FIG. 1. A sketch of a Taylor-Couette flow setup with an axial background magnetic field.

large, where  $L_z$  is the length of the cylinders. For simplicity, here we assume that the cylinders do not have endcaps and perturbations are periodic along the cylinder axis. The ratio of the angular velocities of the outer and inner cylinders,  $\mu = \Omega_{out}/\Omega_{in}$ , can be varied (see Table I). A uniform axial magnetic field  $\mathbf{B}_0 = B_{0z}\mathbf{e}_z$  is imposed by a current-carrying solenoid surrounding the outer cylinder. This field is current-free between the cylinders,  $\mathbf{J}_0 = \mu_0^{-1}\nabla \times \mathbf{B}_0$ , and therefore does not exert any Lorentz force on the fluid. As a result, in the absence of endcaps, the equilibrium azimuthal flow  $\mathbf{U}_0 = (0, r\Omega(r), 0)$  between the cylinders has a classical hydrodynamical TC profile of angular velocity

$$\Omega(r) = C_1 + \frac{C_2}{r^2}$$

where the coefficients  $C_1$  and  $C_2$  are

$$C_1 = \frac{\Omega_{out}r_{out}^2 - \Omega_{in}r_{in}^2}{r_{out}^2 - r_{in}^2}, \quad C_2 = \frac{(\Omega_{in} - \Omega_{out})r_{in}^2r_{out}^2}{r_{out}^2 - r_{in}^2},$$

In laboratory TC experiments, this equilibrium profile is inevitably modified due to Ekman circulations (pumping) induced by the endcaps [14, 25, 40, 41]. This effect for DRESHDYN-MRI experiments will be discussed elsewhere. Here we only note that the DRESHDYN-TC device has a large aspect ratio ( $=10$ ) and split endcap rings designed such as to minimize Ekman pumping [41].

The basic equations of viscous and resistive MHD governing motion of an incompressible conducting fluid are

$$\frac{\partial \mathbf{U}}{\partial t} + (\mathbf{U} \cdot \nabla)\mathbf{U} = -\frac{1}{\rho}\nabla P + \frac{\mathbf{J} \times \mathbf{B}}{\rho} + \nu \nabla^2 \mathbf{U}, \quad (1)$$

$$\frac{\partial \mathbf{B}}{\partial t} = \nabla \times (\mathbf{U} \times \mathbf{B}) + \eta \nabla^2 \mathbf{B}, \quad (2)$$

Dimensionless Parameter	Definition	Values
$\mu$	$\Omega_{out}/\Omega_{in}$	(0.25, 0.35]
Aspect ratio	$L_z/r_{in}$	10
Reynolds number ( $Re$ )	$\Omega_{in}r_{in}^2/\nu$	$\leq 7.72 \times 10^6$
Lundquist number ( $Lu$ )	$B_{0z}r_{in}/\eta\sqrt{\rho\mu_0}$	$\leq 10$
Magnetic Prandtl number ( $Pm$ )	$\nu/\eta$	$7.77 \times 10^{-6}$
Magnetic Reynolds number ( $Rm$ )	$Re \cdot Pm$	$\leq 40$

TABLE I. Non-dimensional system parameters of the DRESHDYN-MRI experiment with liquid sodium at  $T = 130^\circ\text{C}$  (see Paper I).

$$\nabla \cdot \mathbf{U} = 0, \quad \nabla \cdot \mathbf{B} = 0, \quad (3)$$

where  $\rho$  is the constant density,  $\mathbf{U}$  is the velocity,  $P$  is the thermal pressure,  $\mathbf{B}$  is the magnetic field,  $\mathbf{J} = \mu_0^{-1}\nabla \times \mathbf{B}$  is the current density with  $\mu_0$  being the magnetic permeability of vacuum. The fluid has constant kinematic viscosity  $\nu$  and Ohmic resistivity  $\eta$ . The basic TC flow is hydrodynamically stable according to Rayleigh's criterion, i.e.,  $\mu = \Omega_{out}/\Omega_{in} > (r_{in}/r_{out})^2 = 0.25$ , ensuring that all the linear instabilities are of magnetic nature. The values of  $\mu$  are extended up to quasi-Keplerian rotation when cylinders angular velocities are related through Kepler's law,  $\Omega_{out}/\Omega_{in} = (r_{in}/r_{out})^{3/2} \approx 0.35$ , which is of direct relevance for astrophysical disks.

We non-dimensionalize time by  $\Omega_{in}^{-1}$ , angular velocities  $\Omega(r)$  by  $\Omega_{in}$ , length by  $r_{in}$ , velocity  $\mathbf{u}$  by  $r_{in}\Omega_{in}$ , pressure and kinetic energy density by  $\rho\Omega_{in}^2r_{in}^2$  and magnetic field  $\mathbf{B}$  by the background field  $B_{0z}$ . The main parameters are Reynolds number  $Re = \Omega_{in}r_{in}^2/\nu$ , magnetic Reynolds number  $Rm = \Omega_{in}r_{in}^2/\eta$ , magnetic Prandtl number  $Pm = \nu/\eta = Rm/Re$  and Lundquist number  $Lu = V_A r_{in}/\eta$ , where  $V_A = B_{0z}/\sqrt{\rho\mu_0}$  is the Alfvén speed. Table I gives the ranges of these parameters typical of DRESHDYN-MRI experiment, which we use in our subsequent analysis.

### III. LINEAR ANALYSIS OF NON-AXISYMMETRIC SMRI

The linear stability of non-axisymmetric modes is studied around this base TC flow  $\mathbf{U}_0$  with the imposed axial magnetic field  $\mathbf{B}_0$ , against small perturbations,  $\mathbf{u} = \mathbf{U} - \mathbf{U}_0$ ,  $p = P - P_0$ ,  $\mathbf{b} = \mathbf{B} - \mathbf{B}_0$ . We assume these perturbations to have a standard modal form  $\propto \exp(\gamma t + im\phi + ik_z z)$ , where  $\gamma$  is the complex eigenvalue and  $m$  and  $k_z$  are, respectively, the azimuthal and axial wavenumbers. The flow is unstable when the real part of  $\gamma$  is positive,  $\text{Re}(\gamma) > 0$ . Linearizing the main Eqs. (1)-(3), we obtain the system of non-dimensional perturbation equations as given in Paper I. Employing a similar spectral collocation method as in [11, 12], we discretize the radial structure of the variables using the Chebyshev polynomials with typical resolution  $N = 120 - 140$  for a given pair of  $(m, k_z)$ . This resolution is higher than that used for axisymmetric  $m = 0$  SMRI modes in Paper I in order to resolve a thin region around corota-

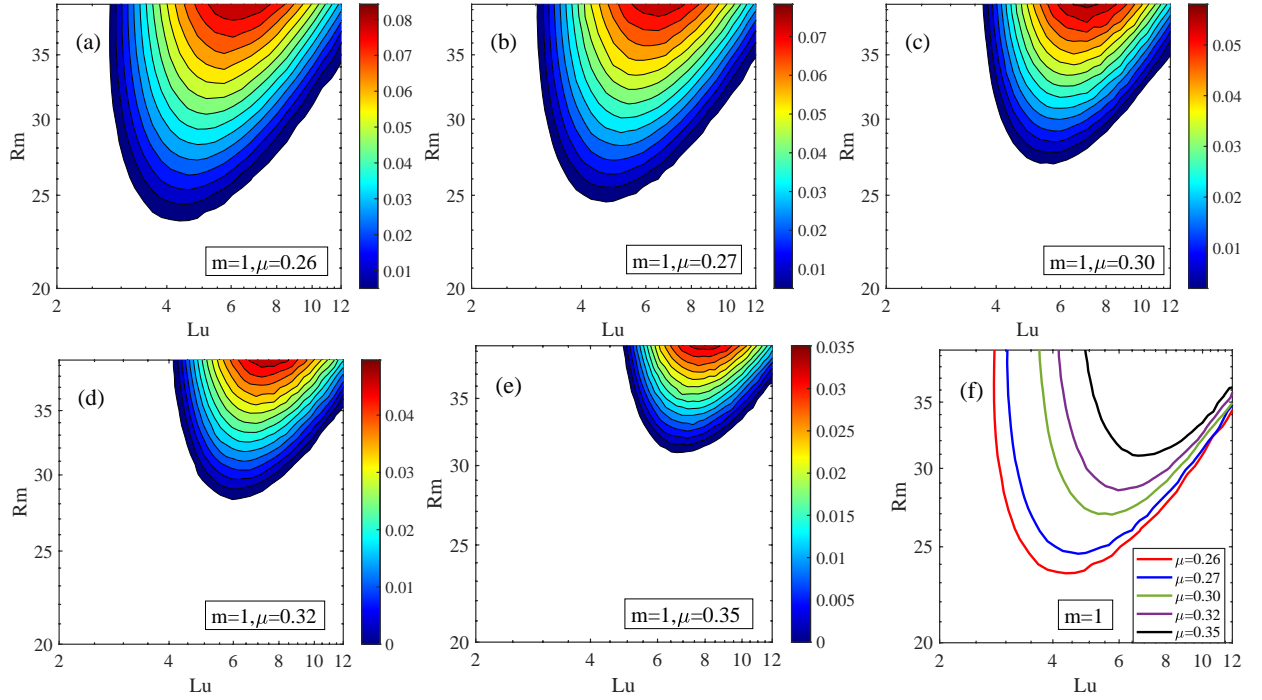


FIG. 2. Growth rate,  $\text{Re}(\gamma) > 0$ , of the non-axisymmetric  $m = 1$  mode of SMRI for  $Pm = 10^{-5}$  and (a)  $\mu = 0.26$ , (b)  $\mu = 0.27$ , (c)  $\mu = 0.30$ , (d)  $\mu = 0.32$ , (e)  $\mu = 0.35$ . (f) The corresponding marginal stability curves for the  $m = 1$  mode at these  $\mu$ .

tion radius  $r_c$ , where  $m\Omega(r_c) = -\text{Im}(\gamma)$ , in the structure of non-axisymmetric  $m \neq 0$  SMRI mode eigenfunctions (see below). Here we assume at least one full axial wavelength of non-axisymmetric modes fits in the cylinder length  $L_z$  ( $= 10$  in non-dimensional units), hence we set for the minimum axial wavenumber  $k_{z,\min} = 2\pi/L_z$  and maximize their growth rate over larger wavenumbers  $k_z \geq k_{z,\min}$ . No slip boundary condition is used for velocity and insulating boundary condition is used for magnetic field. The resulting linear equations together with the boundary conditions constitute a large matrix ( $4N \times 4N$ ) eigenvalue problem for  $\gamma$  and the growth rate of the instability is determined by its real part.

In the linear analysis below, we focus on the non-axisymmetric  $|m| = 1$  SMRI mode, which is the second most unstable after the axisymmetric  $m = 0$  SMRI mode, while higher  $|m| \geq 2$  modes appear to be linearly stable in the considered ranges of the main parameters as given in Table I. On the other hand, in the more interesting fully nonlinear analysis, we include also high- $m$  modes, because, as shown below, they can grow as a result of the modification (deviation) of the radial shear of the mean azimuthal velocity from the initial TC profile due to the nonlinear saturation of the axisymmetric SMRI mode.

We first analyze the growth rate and eigenfunction structure of the non-axisymmetric  $m = 1$  SMRI mode and then make comparison with the axisymmetric mode. Figure 2 shows the growth rate for the unstable non-axisymmetric  $m = 1$  mode, maximized over axial wavenumbers  $k_z \geq k_{z,\min}$ , in the  $(Lu, Rm)$ -plane at  $Pm = 10^{-5}$  and various  $\mu$  [42]. It is seen in this Figure

that, similar to the axisymmetric case studied in Paper I, the instability region for the non-axisymmetric  $m = 1$  SMRI mode moves towards higher  $Lu$  and  $Rm$  with increasing  $\mu$ . This, in turn, increases the critical  $Lu_c$  and  $Rm_c$  for the onset of instability with  $\mu$  (Table II), but nevertheless the critical  $Lu_c \approx 6.7$  and  $Rm_c \approx 30.9$  for the maximum  $\mu = 0.35$  is well within the maximum achievable ranges of Lundquist and magnetic Reynolds numbers in DRESDYN-MRI experiment (Table I). Notably, on comparison with Fig. 2 of Paper I, it is seen that the non-axisymmetric  $|m| = 1$  mode has about 2-3 times smaller growth rate than that of the axisymmetric  $m = 0$  mode for fixed pair of  $(Lu, Rm)$ . At any rate, the non-axisymmetric  $|m| = 1$  SMRI mode for all considered  $\mu \in (0.25, 0.35]$  appears to be unstable within the range of Lundquist and magnetic Reynolds numbers accessible in DRESDYN-TC machine and hence it can in principle be excited in the upcoming DRESDYN-MRI experiment together with the axisymmetric one.

Figure 3 shows the typical structure of the radial and axial velocities,  $(u_r, u_z)$  and magnetic field  $(b_r, b_z)$  eigenfunctions in the  $(r, z)$ -plane for the non-axisymmetric  $m = 1$  mode at  $\mu = 0.35$ ,  $Lu = 7$ ,  $Rm = 37$  and the axial wavenumber  $k_z = 2.23$ , which corresponds to the maximum growth rate at these values of the parameters. The radial and axial velocity eigenfunctions reach their maxima and have a strong elongation of the cells in the axial direction within a thin layer around  $r_c \approx 1.3$ . This point in fact represents the corotation radius at which the azimuthal phase velocity of the mode is equal to the flow velocity, i.e.,  $m\Omega(r_c) = -\text{Im}(\gamma)$ , and is located closer



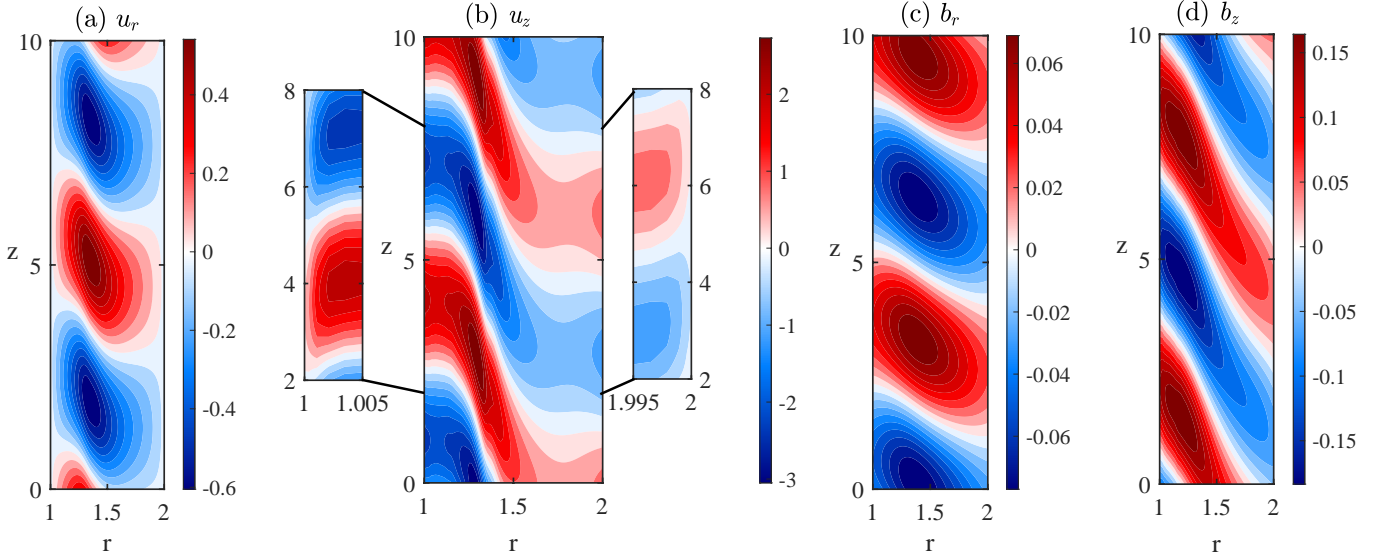


FIG. 3. Structure of the (a) radial velocity  $u_r$ , (b) axial velocity  $u_z$ , (c) radial magnetic field  $b_r$  and (d) axial magnetic field  $b_z$  eigenfunctions in the  $(r, z)$ -plane for  $m = 1$  mode of SMRI at  $\mu = 0.35$ ,  $Lu = 7$ ,  $Rm = 37$ ,  $Pm = 10^{-5}$  and  $k_z = 2.23$ . The eigenfunctions reach maxima around corotation radius (see text). A zoomed version of the axial velocity  $u_z$  at the cylinder boundaries is shown to demonstrate the validity of no slip boundary condition for velocity.

to the inner boundary. This is consistent with the results of Ref. [37] that non-axisymmetric  $m = 1$  SMRI mode eigenfunctions are confined between two Alfvén resonance points located on either side of the corotation radius and reach higher values around that radius [43]. Since it is a higher-frequency mode, its corotation radius and hence the eigenfunctions tend to be located nearer the inner cylinder wall. Similarly, the radial and axial magnetic field eigenfunctions are also elongated near the corotation radius, but to a lesser degree, and reach higher values there.

In the DRESDYN-MRI experiment, large values of  $Lu$  and  $Rm$  are achievable where the axisymmetric and non-axisymmetric modes can co-exist in the flow. Given the importance of definitive detection of these modes, one should determine the parameter ranges over which these axisymmetric  $m = 0$  and non-axisymmetric  $m = 1$  SMRI modes can be uniquely identified. For comparison, in Fig. 4 we show the marginal stability curves for these modes together for different  $\mu \in \{0.27, 0.30, 0.35\}$ . As mentioned above, the instability region for both  $m = 0$  and  $m = 1$  modes in the  $(Lu, Rm)$ -plane becomes smaller and smaller as  $\mu$  increases, because in this case the shear of the basic TC flow, which mainly drives SMRI, decreases. Obviously, the instability region of the axisymmetric  $m = 0$  mode is much larger than that of the non-axisymmetric  $m = 1$  mode, and therefore the critical  $(Lu_c, Rm_c)$  for  $m = 0$  SMRI mode is about 1.3-2.87 and 1.9-4.85 times smaller than those of the non-axisymmetric  $|m| = 1$  modes for fixed  $\mu$  (see Table II and Paper I). Hence, this gap between the  $m = 0$  and  $|m| = 1$  modes critical values at fixed  $\mu$  can be exploited to ensure the detection of axisymmetric SMRI mode dis-

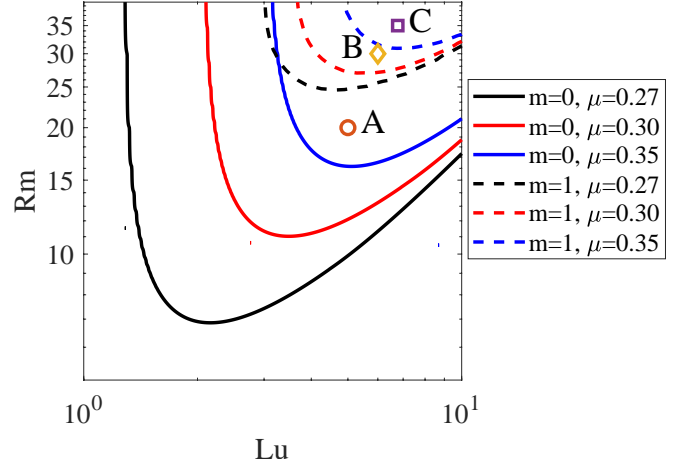


FIG. 4. Marginal stability curves for axisymmetric  $m = 0$  (solid lines) and non-axisymmetric  $m = 1$  (dashed lines) SMRI modes at different  $\mu = 0.27$  (black),  $0.30$  (red),  $0.35$  (blue). For all  $\mu$ ,  $m = 0$  mode has much lower critical  $Lu_c$  and  $Rm_c$  than the  $m = 1$  mode. Points A, B, and C, which lie, respectively, outside, near and inside the marginal stability curve of the  $m = 1$  mode for the classical TC profile with quasi-Keplerian rotation  $\mu = 0.35$ , are used for the subsequent nonlinear analysis.

tinct from non-axisymmetric one.

$\mu$	$(Lu_c, Rm_c)$	
	$m = 0$	$ m  = 1$
0.26	(1.5, 4.8)	(4.3, 23.3)
0.27	(2.1, 6.9)	(4.7, 24.5)
0.30	(3.5, 11)	(5.7, 26.9)
0.32	(4.2, 13.2)	(5.9, 28.5)
0.35	(5.1, 16.2)	(6.7, 30.9)

TABLE II. Critical values for the onset of axisymmetric  $m = 0$  and non-axisymmetric  $|m| = 1$  SMRI modes for different  $\mu$  obtained via linear stability analysis.

#### IV. NONLINEAR EVOLUTION OF NON-AXISYMMETRIC MODES

From the linear stability analysis, we inferred that the axisymmetric and non-axisymmetric SMRI modes can coexist in the same parameter regime with the latter typically having several times lower growth rates. In the experiments, flow is allowed to reach a steady state before the measurements are done. Thus, in order to uniquely identify different modes in the flow, it is necessary to first understand the nonlinear saturation properties of both axisymmetric and non-axisymmetric modes. In Paper II, we studied the nonlinear saturation and dynamics of axisymmetric SMRI mode, since it is the most unstable SMRI mode in the considered TC flow. We showed that it saturates via magnetic reconnection and derived, both analytically and numerically, the scaling relations of the volume-integrated magnetic energy and perturbed torque at the cylinders in the saturated state with respect to Reynolds number  $Re$ . Importantly, these scalings have allowed us to extrapolate and estimate the expected magnitudes of velocity and magnetic field perturbations at those high  $Re \gtrsim 10^6$  which are relevant for the DRESHDYN-MRI experiment. While Paper II specifically focused on axisymmetric SMRI mode, this section investigates the nonlinear evolution and saturation of non-axisymmetric modes in comparison with axisymmetric ones, which is important for the preparation of the DRESHDYN-MRI experiment.

To solve the basic non-ideal MHD Eqs. (1)-(3), as in Paper II, we use the pseudo-spectral code described in [44]. This code employs a high-order finite-difference method for radial expansion, and Fourier expansions for axial and azimuthal directions. The time-update is done using an implicit Crank-Nicolson approach of second order. The nonlinear terms are calculated using the pseudo-spectral method, and the 3/2-rule is applied for de-aliasing. As in the linear analysis above, the boundary conditions are no-slip for velocity and insulating for magnetic field at the cylinder walls, which is consistent with the conditions present in the DRESHDYN-MRI facility, and periodic in the axial direction. Additional details about this code and its validation can be found in [44]. The cylindrical flow domain is defined by the coordinates

$(r, \phi, z) \in [r_{in}, r_{out}] \times [0, 2\pi] \times [0, L_z]$ , where the non-dimensional inner and outer radii  $r_{in} = 1$ ,  $r_{out} = 2$ , and the cylinder length  $L_z = 10$ . To achieve high resolution close to the cylinder walls, the Chebyshev collocation method is used to distribute points radially. We take  $N_r = 480$  finite difference points in the radial direction and  $N_z = 480$  Fourier modes in the axial direction, providing high enough resolution for the modes. The total number of non-axisymmetric modes,  $N_\phi$ , is set to 20, that is, the azimuthal wavenumber  $|m| \in [0, 20]$ . We conducted the resolution study in order to optimize  $N_\phi$  and found that  $N_\phi = 20$  is sufficient to reach convergence of the  $m$ -spectra and hence to reliably capture the dynamics of non-axisymmetric modes (see Fig. 14 in Appendix 1). As in the linear analysis, the minimum axial wavelength is set to  $k_{z,min} = 2\pi/L_z$  to ensure at least one full wavelength fits in the axial direction.

##### A. Magnetic energy – evolution and radial dependence

Figure 5 shows the time-evolution of the volume-integrated magnetic energy density of perturbations,  $\mathcal{E}_{mag} = \frac{1}{2} \int_V \mathbf{b}^2 dV$ , where  $V$  is the volume of the TC flow domain, for axisymmetric  $m = 0$  mode, summed over non-axisymmetric  $|m| \geq 1$  modes and the total magnetic energy for all  $|m| \geq 0$  modes at  $\mu = 0.35$ ,  $Lu = 5$ ,  $Rm = 20$  (point A in Fig. 4) and different  $Re = \{3, 4, 6\} \times 10^4$ . It is seen in Fig. 4 that point A is way outside the linearly unstable regime of the  $m = 1$  mode in the presence of the original TC profile but still falls in the linearly unstable regime of  $m = 0$  SMRI mode. At  $Re = 3 \times 10^4$ , the magnetic energy of non-axisymmetric modes decays over time while the axisymmetric mode grows and saturates [Fig. 5(a)]. For higher  $Re = 4 \times 10^4$  shown in Fig. 5(b), the magnetic energy of the non-axisymmetric modes initially decays during the exponential growth phase of the axisymmetric mode, but then increases very rapidly during the saturation process of the latter mode. However, after the axisymmetric mode has saturated, this peak in the non-axisymmetric mode energy is not sustained and decays afterwards, settling down to a very small noise level. A similar peak in the evolution of the non-axisymmetric mode energy is seen for even higher  $Re = 6 \times 10^4$  shown in Fig. 5(c), but in this case the non-axisymmetric mode energy eventually saturates at orders of magnitude higher levels, though still a few orders lower than the energy level of the axisymmetric mode. This indicates that depending on  $Re$  the non-axisymmetric modes, which would be stable for classical TC profile, can nevertheless undergo rapid growth and saturate just during the saturation process of the axisymmetric modes. A similar trend is seen at  $Lu = 6$ ,  $Rm = 30$  marked as point B in Fig. 4, where the non-axisymmetric modes are marginally stable initially and become unstable in the course of saturation of the axisymmetric mode, as seen in Fig. 15 of Appendix 2. Note that in all these

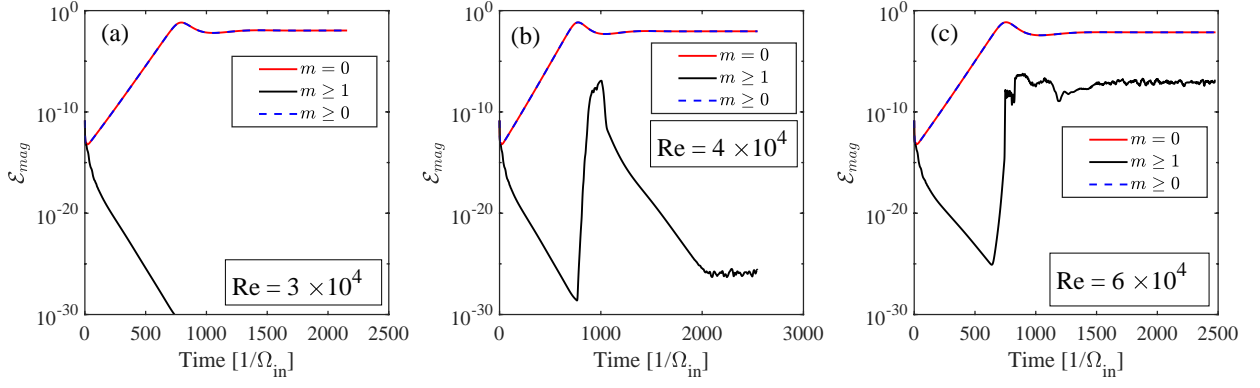


FIG. 5. Time evolution of volume-integrated magnetic energy  $\mathcal{E}_{mag}$  for  $Lu = 5$ ,  $Rm = 20$ , corresponding to point A in Fig. 4 and  $Re = 3 \times 10^4$  (a),  $4 \times 10^4$  (b) and  $6 \times 10^4$  (c). The non-axisymmetric modes are linearly stable and hence initially decay for all  $Re$  in the exponential growth phase of the axisymmetric SMRI mode. Rapid transient growth of non-axisymmetric modes occur at large enough  $Re$  (or small  $Pm$ ) as seen in (b) and (c), which is due to the change, or deviation of the mean azimuthal flow profile from the initial TC flow as a result of the saturation of the dominant axisymmetric mode. At  $Re = 6 \times 10^4$ , the non-axisymmetric modes' energy does not decay after the growth and settles down to a constant value, which is still several orders smaller than that of axisymmetric mode.

cases the axisymmetric mode is a dominant contributor to the total magnetic energy of the flow.

The time-evolution of the volume-integrated magnetic energy for  $Lu = 6.78$ ,  $Rm = 35$  (point C in Fig. 4), and at  $Re = \{1, 2, 4\} \times 10^4$  are shown in Fig. 6. Since the point C falls well within the linearly unstable regime, we see an initial exponential growth phase of the non-axisymmetric mode. The growth rate obtained from the nonlinear code is  $\sim 0.012$  which is similar to that from the linear code  $\sim 0.015$  for all  $Re$  discussed in Fig. 6. Hence, it can be inferred that the unstable  $|m| = 1$  mode exhibiting growth at early times in the simulations is in fact the SMRI mode. For  $Re = 10^4$  and  $2 \times 10^4$  shown in Figs. 6(a) and 6(b), the non-axisymmetric modes do not, however, saturate after the exponential growth, but instead start to decrease during the saturation process of the axisymmetric SMRI mode; at  $Re = 2 \times 10^4$  this decrease is followed by some transient amplification, which reaching a maximum, falls again. By contrast, at larger  $Re = 4 \times 10^4$ , the magnetic energy of the non-axisymmetric modes, after an initial exponential growth phase, increases much more steeply during the saturation of the axisymmetric mode and eventually saturates itself to a certain value few orders smaller than that of the axisymmetric mode [Fig. 6(c)]. Figures 5 and 6 thus indicate that at high enough  $Re$  non-axisymmetric modes exhibit rapid amplification in the nonlinear regime, irrespective of their initial linear stability or instability, when the dominant axisymmetric mode saturates.

To qualitatively analyze the growth and saturation of a non-axisymmetric mode with a given  $m$ , we define a radially integrated spectral magnetic energy density [45],

$$\hat{\mathcal{E}}_{mag}(m, k_z) = \pi L_z \int_{r_{in}}^{r_{out}} (|\bar{b}_r|^2 + |\bar{b}_\phi|^2 + |\bar{b}_z|^2) r dr, \quad (4)$$

where  $\bar{b}_i$ ,  $i \in r, \phi, z$  are the Fourier transforms of the

perturbation magnetic field components in the azimuthal and axial directions,

$$\bar{b}_i(r, m, k_z) = \frac{1}{2\pi L_z} \int_0^{2\pi} \int_0^{L_z} b_i(r, \phi, z) e^{-im\phi - ik_z z} d\phi dz. \quad (5)$$

Using relation (4) we define the azimuthal  $m$ -spectrum of the magnetic energy density as the sum of  $\hat{\mathcal{E}}_{mag}(m, k_z)$  over all  $k_z$ , i.e.,  $\mathcal{E}_{mag}(m) = \sum_{k_z} \hat{\mathcal{E}}_{mag}(m, k_z)$  and study the time evolution of each  $m$ -mode separately. In Fig. 7, we plot the time evolution of  $\mathcal{E}_{mag}(m)$  for different  $m \in [0, 14]$  modes at the same parameters as in Fig. 6. From Fig. 7, it is evident that in the initial linear regime the exponential growth of the total magnetic energy of non-axisymmetric modes depicted in Fig. 6 is essentially dominated by the  $m = 1$  mode while all other  $|m| > 1$  modes are stable and their energies decrease. For smaller  $Re = 10^4$ , the  $m = 1$  mode also starts to decay to a very small noise level, as the axisymmetric  $m = 0$  mode undergoes the saturation phase and modifies the mean azimuthal flow profile [Fig. 7(a)]. For larger  $Re = 2 \times 10^4$  shown in Fig. 7(b), all non-axisymmetric  $|m| \geq 1$  modes exhibit transient growth nearly at the same time of the axisymmetric mode saturation. This transient growth lasts the longer and reaches the higher peaks, the smaller  $m$  is and then decays again to a very small level. Interestingly, for even higher  $Re = 4 \times 10^4$  transition to a nonlinear (turbulent) state finally takes place – all  $m \geq 1$  modes are excited, growing now rapidly during the same time of the axisymmetric mode saturation, and settle down to nearly similar amplitudes due to strong mutual nonlinear interaction at such high  $Re$  [Fig. 7(c)]. (A similar behavior is observed also at point B near the marginal stability curve in Fig. 4 and is discussed in Appendix 2, see Fig. 16). Note that in all the cases considered above the saturation level of non-axisymmetric modes is

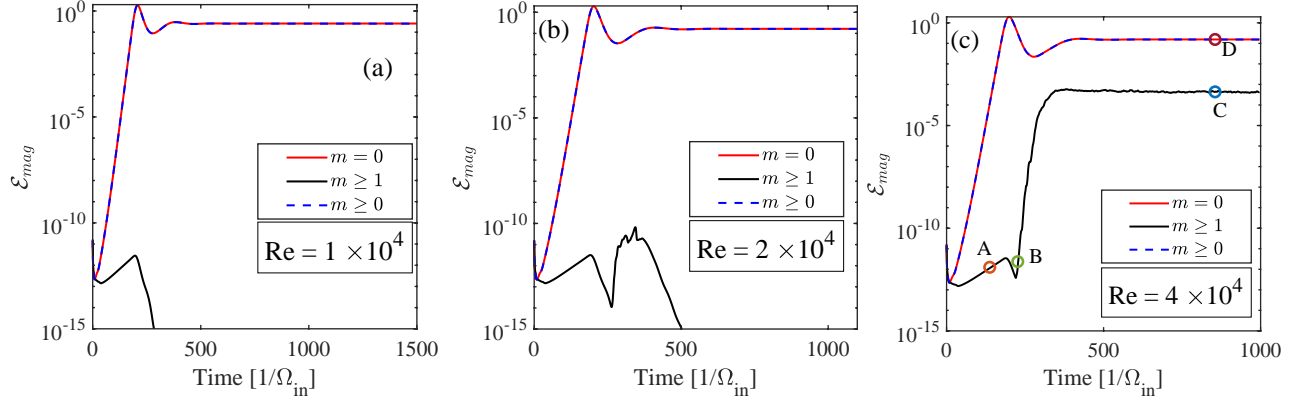


FIG. 6. Same as in Fig. 5 but for  $Lu = 6.78, Rm = 35$ , corresponding to point C in Fig. 4, and  $Re = 10^4$  (a),  $2 \times 10^4$  (b) and  $4 \times 10^4$  (c). Note that the point C is inside the marginal stability curve of  $m = 1$  mode obtained from the original TC profile and therefore this mode grows for all  $Re$  in the initial linear regime. As in Fig. 5, much steeper amplification of the non-axisymmetric mode energy occurs at higher  $Re$  during the saturation of the axisymmetric mode as seen in (b) and (c), which in the latter case does not decay and saturates at a constant value. Points A, B, C and D on the non-axisymmetric and total energy curves in panel (c) will be used in subsection IV B.

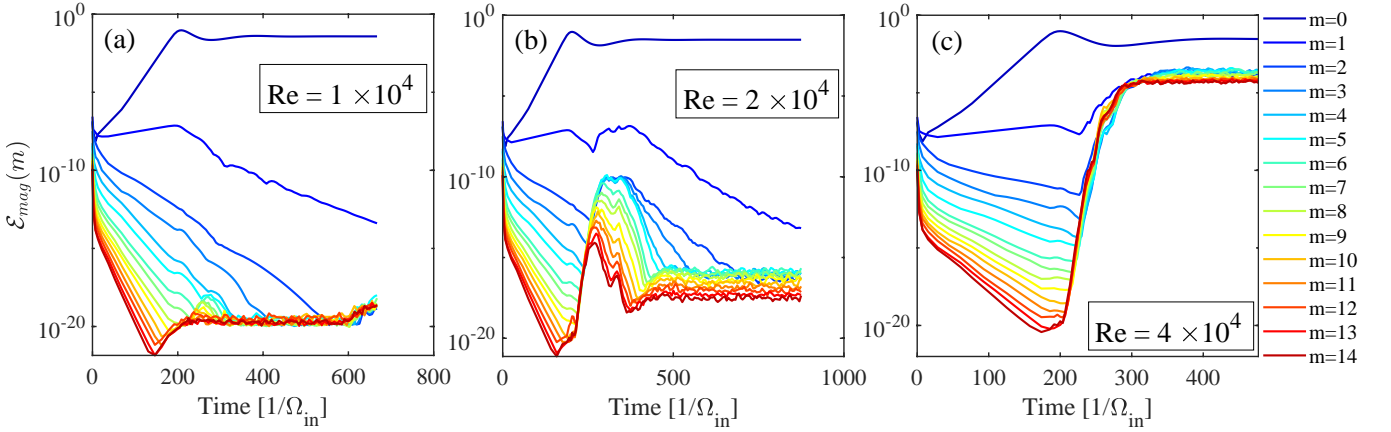


FIG. 7. Time evolution of the azimuthal spectral magnetic energy density  $\mathcal{E}_{mag}(m)$  for different  $m \in [0, 14]$  at the same  $Lu = 6.78, Rm = 35$  and  $Re$  as in Fig. 6. In the initial linear regime, non-axisymmetric  $|m| > 1$  modes decay for all  $Re$  while  $m = 1$  mode grows exponentially, because the point C lies in the unstable regime of this mode. For the smallest  $Re$ , all the non-axisymmetric  $m \geq 1$  modes eventually decay in the saturated state. These modes undergo rapid growth at higher  $Re$  during the saturation of the axisymmetric mode. This growth is only transient at  $Re = 2 \times 10^4$  and decays to a noise level, but saturates at  $Re = 4 \times 10^4$  at about the same level though orders of magnitude smaller than that of the axisymmetric one.

few orders of magnitude smaller than that of the axisymmetric one. This indicates that the axisymmetric SMRI is always a dominant mode in the TC flow for the considered ranges of the main parameters ( $Lu, Rm$ ) relevant to DRES-DYN-MRI experiment and as high  $Re$  (i.e., as small  $Pm$ ) as we can afford in our numerical simulations.

To investigate the radial structure of the non-axisymmetric modes with higher  $|m| \geq 1$  in the saturated state, using Eq. (5) we compute  $b^2(r, m) = \sum_{k_z} \bar{b}_i^2(r, m, k_z)$ ,  $i \in \{r, \phi, z\}$ , which effectively gives the axially integrated magnetic energy. Figure 8 shows  $b^2(r, m)$  as a function of radius  $r$  in the saturated state at high  $Re = 4 \times 10^4$  and  $6 \times 10^4$  at points B and C in Fig. 4. In both Figs. 8(a) and 8(b) it is seen that, in the saturated state, the non-axisymmetric modes are generally

concentrated near the inner cylinder wall, with higher- $m$  modes tend to be more confined to the wall, indicating an important role of boundaries in the dynamics of these modes. In Paper II, we demonstrated that the saturation of the axisymmetric SMRI mode occurs via magnetic reconnection and results in the modification of the mean azimuthal flow profile from a standard TC profile. This modified flow profile involves steep velocity gradients at the cylinder walls which lead to the development of a specific boundary layer. At high  $Re$ , the boundary layers become thinner and the velocity gradients therein, characterized by the local shear parameter  $q = -\partial \ln \Omega / \partial \ln r$ , steeper as shown in Fig. 8(c) of Paper II. As a result, the boundary layers become Rayleigh-unstable with high  $q$  values (much more than the Rayleigh-stability limit

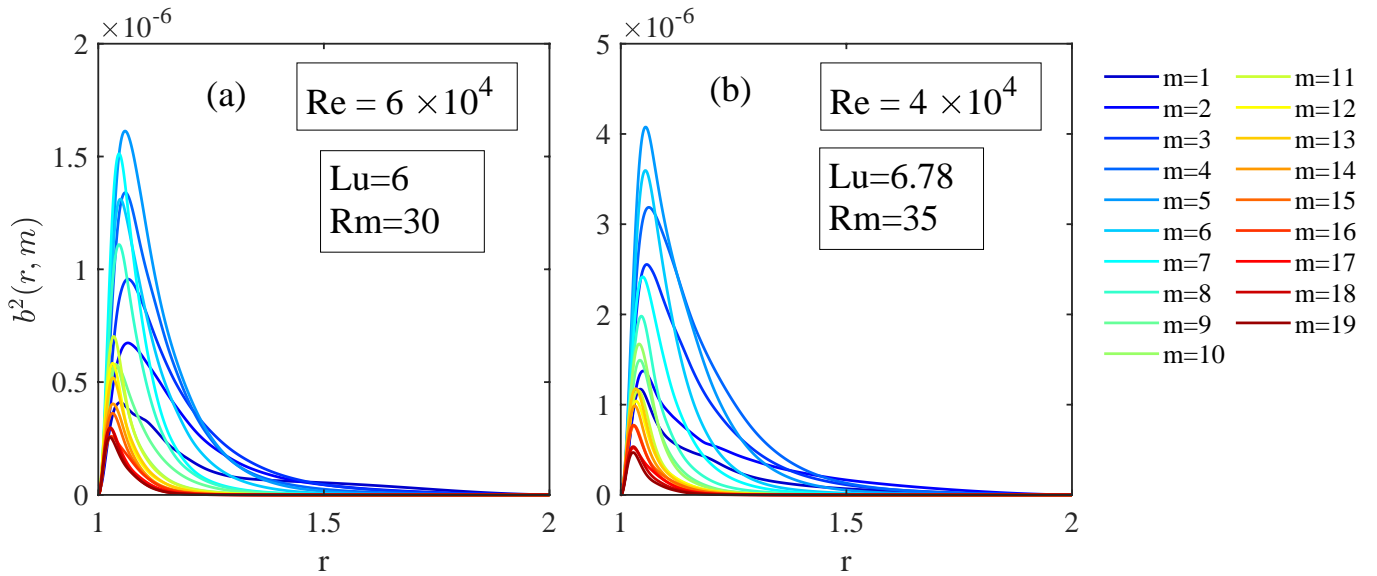


FIG. 8. Axially integrated magnetic energy  $b^2(r, m)$  as a function of  $r$  in the saturated state at different  $m \in [1, 19]$  for  $Lu = 6, Rm = 30, Re = 6 \times 10^4$  (a) and  $Lu = 6.78, Rm = 35, Re = 4 \times 10^4$  (b) corresponding to points B and C in Fig. 4, respectively. From (a) and (b) it is clear that the larger- $m$  non-axisymmetric modes are more concentrated near the inner cylinder, indicating that they are mainly sustained by high shear  $q$  values at the boundaries.

$q = 2$ ) and eventually break down into turbulence, which develops first near the inner cylinder (see distribution of  $q$  in Fig. 9). The higher- $m$  modes, whose total energy evolution at different  $Re$  has been analyzed above in Figs. 6 and 7, thus all first emerge and grow within the turbulent boundary layer at the inner wall and, being the main ingredients of this turbulence, determine its dynamical properties and spectral content. So, the boundary layers formed as a result of the saturation of the axisymmetric SMRI mode are prone to secondary hydrodynamic (but modified by magnetic field) instability, which renders this layer turbulent wherein the non-axisymmetric modes are mainly localized and maintained via energy extraction from high shear in this layer and mutual nonlinear interactions. This also indicates that the saturation mechanisms of axisymmetric and non-axisymmetric modes are different: the axisymmetric mode saturates via magnetic reconnection, as analyzed extensively in Paper II, and more or less keeps its overall laminar structure except for boundary layers (see also Fig. 9 below), whereas the non-axisymmetric modes, confined near walls, saturate in boundary layer turbulence.

### B. Structure of the nonlinear states

To better illustrate the evolution and saturation process of non-axisymmetric modes in the boundary layers described in the above subsection, in Fig. 9 we show the radial and axial velocity,  $(u_r, u_z)$ , and magnetic  $(b_r, b_z)$  field structures for only non-axisymmetric  $|m| \geq 1$  modes and for all  $|m| \geq 0$  modes in the  $(r, z)$ -plane for  $Lu = 6.78, Rm = 35$  and  $Re = 4 \times 10^4$  at differ-

ent evolution moments marked with points B, C and D in Fig. 6(c). Point A in this figure marks the exponential growth phase of only non-axisymmetric  $|m| \geq 1$  modes in the linear regime when their overall  $(r, z)$ -structure is nearly similar to that obtained from the linear stability analysis for the dominant  $|m| = 1$  mode (Fig. 3), so we give it only in Appendix 3.

Figures 9(a)-9(d) show the structures composed of all non-axisymmetric  $|m| \geq 1$  modes at the beginning of their rapid growth phase [point B in Fig. 6(c)]. It can be seen clearly that, in stark contrast to the eigenfunction structure (Fig. 3), at this time, the strong non-axisymmetric perturbations of velocity [(a), (b)] and magnetic field [(c), (d)] gradually emerge near the inner cylinder boundary. A closer look at the local shear parameter  $q$  in Fig. 9(e) show the disrupting laminar boundary layers due to localized non-axisymmetric perturbations – turbulent spots, indicating that these boundary layers are gradually becoming turbulent [see a zoomed segment in Fig. 9(e)]. Figures 9(f)-9(i) show the velocity and magnetic field structures for these non-axisymmetric modes at later times in the saturated state [point C in Fig. 6(c)] when they are well developed near the inner wall and are clearly visible. The boundary layers are consequently fully turbulent [Fig. 9(j)].

Figures 9(k)-9(n) show the structure of velocity and magnetic fields for all  $m$  modes in the saturated state [point D in Fig. 6(c)]. Evidently, they are dominated by the axisymmetric  $m = 0$  mode and therefore are similar to those analyzed in Paper II (see Fig. 4), exhibiting the typical radial jet [Fig. 9(k)] and thin reconnection layer seen in the magnetic field map where the radial fields with opposite directions meet resulting in high azimuthal

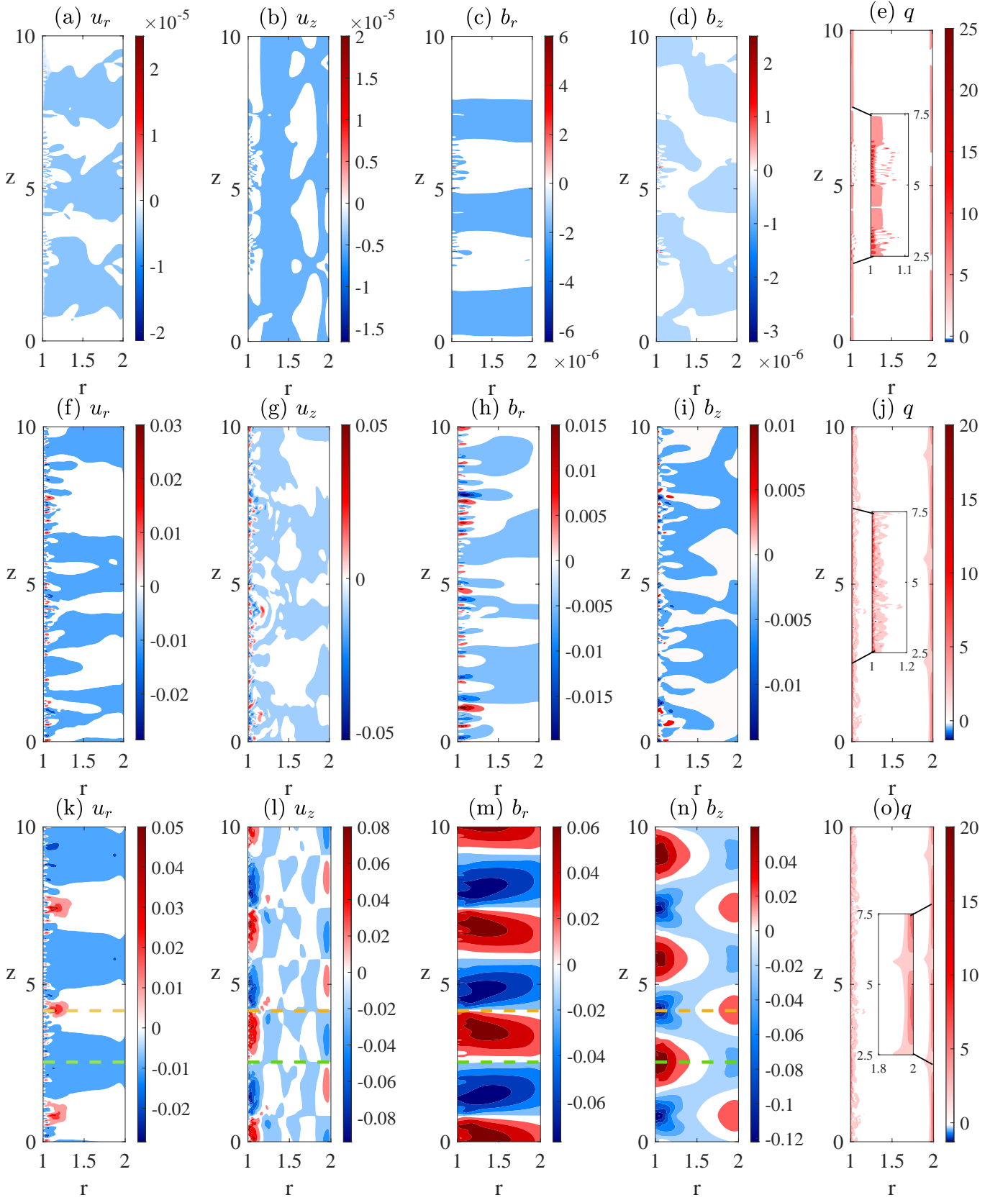


FIG. 9. Radial and axial velocity ( $u_r$ ,  $u_z$ ) and magnetic ( $b_r$ ,  $b_z$ ) field structures in the  $(r, z)$ -plane for  $Lu = 6.78$ ,  $Rm = 35$  and  $Re = 4 \times 10^4$  at different evolution times of axisymmetric and non-axisymmetric modes marked by points B, C and D in Fig. 6. (a)-(d) and (f)-(i) show only non-axisymmetric modes at points B and C, respectively. (k)-(n) show all the modes in the saturated state at point D. Rightmost panels (e), (j) and (o) show the distribution of the local shear parameter  $q = -\partial \ln \Omega / \partial \ln r$  in the  $(r, z)$ -plane. Orange and green dashed lines are plotted at  $z = 4.16$  and  $z = 2.52$  and analysed in Fig. 11 and 12, respectively.



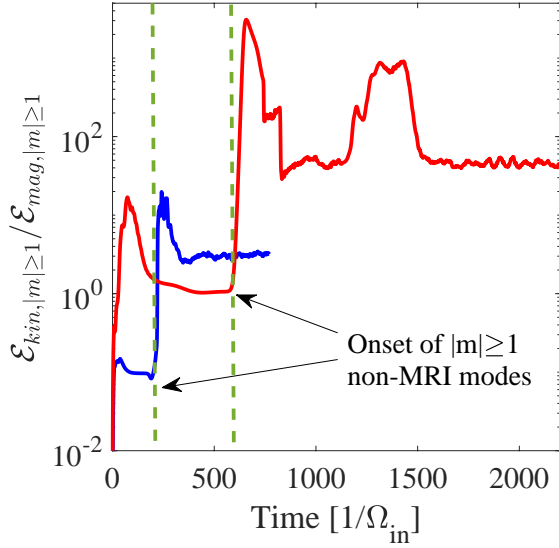


FIG. 10. Time evolution of the ratio of the kinetic to magnetic energies of non-axisymmetric modes,  $\mathcal{E}_{kin,|m|\geq 1}/\mathcal{E}_{mag,|m|\geq 1}$  for  $(Lu, Rm, Re) = (5, 20, 6 \times 10^4)$  (red) and  $(6.78, 35, 4 \times 10^4)$  (blue) corresponding to Fig. 5 and 6, respectively. Dashed green lines mark the onset point of non-axisymmetric non-MRI modes.

current density there [Fig. 9(m)]. These are the main players in the saturation dynamics of the axisymmetric SMRI studied in detail in Paper II.

From the above analysis, we conclude that these small-scale non-axisymmetric modes, which emerge and grow after the saturation of the dominant axisymmetric SMRI mode and survive in the saturated state, are *not* SMRI modes. Instead, these are the non-axisymmetric modes excited in the Rayleigh-unstable (turbulent) boundary layers, which, as mentioned above, arise as a result of the saturation process of the axisymmetric SMRI mode. The passive magnetic field perturbations in these modes arise as a result of velocity perturbations advecting the imposed axial magnetic field. Figure 10 gives an additional confirmation of the nonmagnetic nature of these modes. It shows the time evolution of the ratio of the total kinetic to magnetic energies of non-axisymmetric modes,  $\mathcal{E}_{kin,|m|\geq 1}/\mathcal{E}_{mag,|m|\geq 1}$ , for the parameters used in Figs. 5 and 6, respectively. In the initial exponential growth phase, the non-axisymmetric modes are SMRI modes, so this ratio is almost constant, as is typical of the normal mode, and the kinetic energy is smaller or comparable to the magnetic energy. However, once the axisymmetric SMRI mode starts to saturate and modify the mean azimuthal flow profile, the kinetic energy shoots up orders of magnitude higher over the magnetic energy (indicated with green dashed lines), signalling the onset of non-MRI/magnetic non-axisymmetric modes in the flow. During the subsequent evolution their kinetic energy remains always larger than the magnetic energy by a factor which is higher at higher  $Re$ . Since these modes are nonmagnetic in nature, they can, in princi-

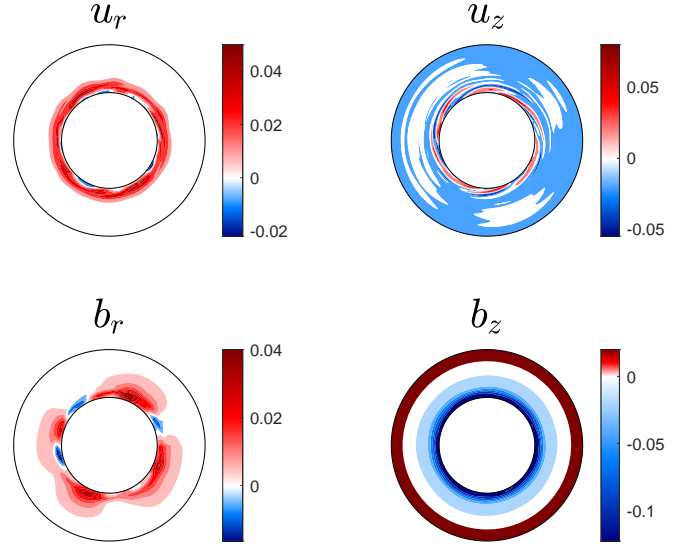


FIG. 11. Radial and axial velocity ( $u_r, u_z$ ) and magnetic ( $b_r, b_z$ ) fields in the  $(r, \phi)$ -plane at axial length  $z = 4.16$  shown by orange dashed line in the bottom row of Fig. 9 for  $Lu = 6.78$ ,  $Rm = 35$  and  $Re = 4 \times 10^4$  in the saturated state.

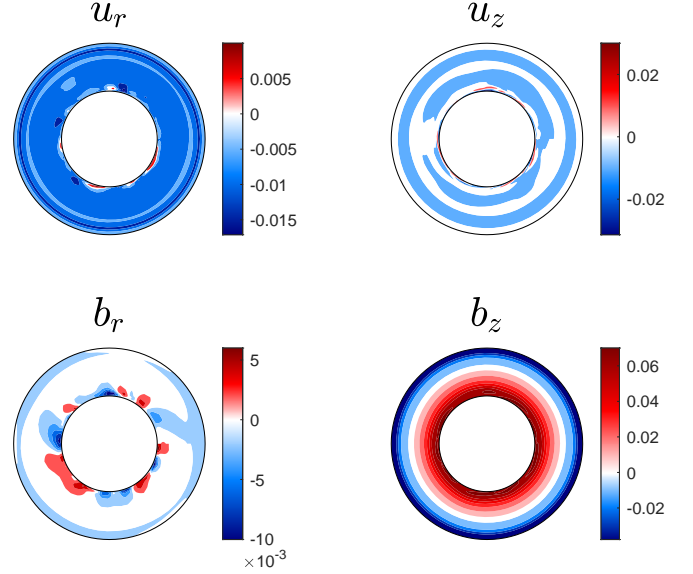


FIG. 12. Same as Fig. 11 but at axial length  $z = 2.52$  shown by the green dashed line in the bottom row of Fig. 9

ple, appear subcritically in the presence of original TC flow for those  $Lu$  and  $Rm$  which are linearly stable for non-axisymmetric SMRI but unstable for axisymmetric SMRI for large enough  $Re$  as evident from Fig. 5.

In Fig. 11, we plot the perturbed total (including all  $m$ ) radial and axial velocity ( $u_r, u_z$ ) and magnetic ( $b_r, b_z$ ) fields in the  $(r, \phi)$ -plane at axial length  $z = 4.16$  marked by orange dashed line in Fig. 9 for the same parameters. The axial length  $z = 4.16$  is chosen such that the extent of velocity and magnetic field at the site of radial jet and magnetic reconnection can be analysed

qualitatively in the meridional plane. The radial velocity  $u_r$ , shown in Fig. 11, is strongly concentrated along the inner cylinder. Since  $u_r$  is positive at the inner boundary, the jet travels from the inner cylinder towards outer one with an effective penetration radius  $r \sim 1.3$  and is negligible elsewhere. The radial magnetic field  $b_r$  originates due to instability and is concentrated predominantly near the inner cylinder and is nearly zero elsewhere. However, the axial velocity  $u_z$  is sheared (or spiralled) axially along inner cylinder with up-down motion very close to inner cylinder while bulk of the flow is either stationary or moving slowly downward. The perturbed axial magnetic field  $b_z$ , is mostly concentrated along the inner and outer cylinders and directed oppositely, while in the bulk of the flow  $b_z$  is nearly zero.

Figure 12 shows the radial and axial velocity ( $u_r, u_z$ ) and magnetic ( $b_r, b_z$ ) fields in the  $(r, \phi)$  plane for the same parameters as in Fig. 11 but at axial length of  $z = 2.52$  marked as green dashed line in Fig. 9, which is chosen such that the effect of the radial velocity jet (or magnetic reconnection) is minimal and is representative of the bulk flow between successive jets. In contrast to the radial velocity jet  $u_r$  in Fig. 11, the radial velocity  $u_r$  is slightly perturbed very close to inner cylinder due to non-axisymmetric modes and the bulk flow moves radially from outer to inner cylinder as shown in Fig. 12. A similar trend is seen for axial velocity  $u_z$ . Perturbed radial and axial magnetic field  $b_r$  and  $b_z$ , respectively, are mostly concentrated near the inner cylinder with very small perturbations of magnetic field in the bulk flow.

### C. Scalings of magnetic energy and torque with $Re$

The emergence of non-axisymmetric non-MRI modes during the saturation process of the axisymmetric SMRI mode naturally gives rise to the question whether the  $Re$ -scalings of saturated state magnetic energy and torque reported in Paper II still holds well or not. Of particular interest is the influence of non-axisymmetric modes on the empirical scaling relation between the saturated state's magnetic energy and normalised perturbation to torque,  $(\hat{\mathcal{E}}_{mag})^{-1}(G/G_{lam} - 1) \sim Re$ , which was observed to hold for all studied parameters in Paper II. To verify the scaling relations in the presence of non-axisymmetric modes, in Fig. 13(a) we plot the total (summed over all  $m$ ) magnetic energy  $\hat{\mathcal{E}}_{mag}$  as a function of  $Re$  for  $(Lu, Rm) = (5, 20)$  and  $(6.78, 35)$  in the saturated state. In the first case, for  $Re \lesssim 2 \times 10^4$ , the scaling of the magnetic energy follows  $Re^{-0.55}$ , while in the second case  $\sim Re^{-0.6}$ , which are similar to those reported for purely axisymmetric SMRI in Paper II. Interestingly, for higher  $Re \gtrsim 2 \times 10^4$  [marked by the vertical red dotted line in Fig. 13(a)], the scaling of  $\hat{\mathcal{E}}_{mag}$  changes to less steep  $Re^{-0.4}$  for  $(Lu, Rm) = (6.78, 35)$ , which is due to the excitation of non-axisymmetric modes through the secondary instability of the azimuthal velocity that sets on just at such high  $Re \gtrsim 2 \times 10^4$  [see Figs. 6(c) and 13(c)].

At this  $Lu$  and  $Rm$ , the non-axisymmetric modes turn out to be strong enough so that their nonlinear back reaction on the dominant axisymmetric mode modifies its scaling behavior at high  $Re$  (see below). On the other hand, the scaling for smaller  $(Lu, Rm) = (5, 20)$  remains the same across all Reynolds numbers, as evident from the blue line in Fig. 13(a). This is because the saturated energy of non-axisymmetric modes is several orders smaller than that for larger  $Lu$  and  $Rm$  [green curve in Fig. 13(a) and Fig. 18].

Let us now look at the behavior of the total torque with Reynolds number. Figure 13(b) shows the normalized torque due to perturbations or *simply* torque  $G/G_{lam} - 1$  for the same parameters as in Fig. 13(a). At  $Re \lesssim 2 \times 10^4$ , the scaling of the torque for smaller  $(Lu, Rm) = (5, 20)$  follows  $Re^{0.45}$ , while for larger  $(Lu, Rm) = (6.78, 35)$  it follows  $Re^{0.4}$  in agreement with the scaling in Paper II, whereas at higher  $Re \gtrsim 2 \times 10^4$  [marked by the vertical red dotted line in Fig. 13(b)], only the scaling at  $(Lu, Rm) = (6.78, 35)$  changes to steeper  $Re^{0.56}$ , like for  $\hat{\mathcal{E}}_{mag}$ . Nevertheless, we emphasize that in all cases these findings obey the scaling relation  $(\hat{\mathcal{E}}_{mag})^{-1}(G/G_{lam} - 1) \sim Re$  noted above. This underscores the robustness of this relation and is consistent with the conclusions drawn from the detailed analysis of solely axisymmetric simulations in Paper II. In our simulations, we observed that having a high  $Re$  alone is not sufficient to modify the above-obtained scaling laws due to the secondary instabilities in the flow (at least for the cases we were able to study in our simulations), but  $Lu$  and  $Rm$  should also be high enough, as seen in the scalings of  $\hat{\mathcal{E}}_{mag}$  and  $G/G_{lam} - 1$  in Figs. 13(a) and 13(b).

We demonstrated in Paper II that the saturation of axisymmetric SMRI and corresponding scalings of the magnetic energy and torque are determined by the interplay between the magnetic reconnection and boundary layer dynamics, where the former is characterized by  $Lu$ ,  $Rm$  and latter by  $Re$ . As we have seen above the scaling exponents derived in that study assuming stable (non-turbulent) boundary layer well carry over in the 3D case at lower  $Re \lesssim 2 \times 10^4$ , where non-axisymmetric modes do not survive. On the other hand, at higher  $Re \gtrsim 2 \times 10^4$  small-scale non-axisymmetric, non-MRI modes develop in the inner boundary layer and render it turbulent with different  $Re$ -scaling than that in the laminar boundary layer. This in turn affects the scaling behavior of the saturated SMRI state in the present 3D case, causing a slight deviation of the scaling exponents at high  $Re$  from those of the axisymmetric SMRI obtained in Paper II, as observed above. However, it is seen from Fig. 13 that this effect of the non-axisymmetric modes appears to depend not only on  $Re$ , but also on the  $Lu$  and  $Rm$ , being more appreciable at higher values of these numbers.

It is now interesting to examine whether the non-axisymmetric modes themselves adhere to any specific scaling behaviour. Figure 13(c) shows the evolution of the volume-integrated magnetic energy of all non-axisymmetric  $|m| \geq 1$  modes for  $(Lu, Rm) = (6.78, 35)$

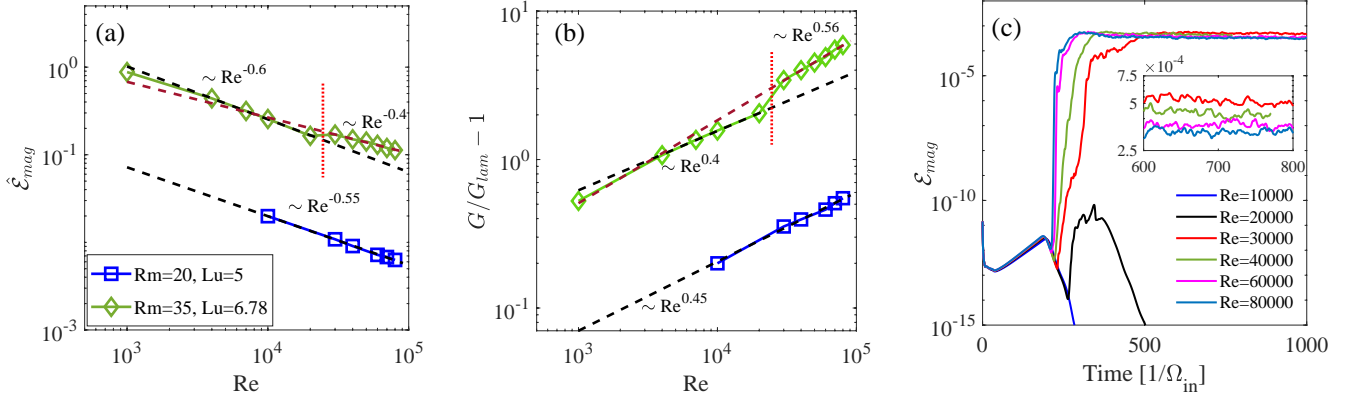


FIG. 13. (a) Volume-integrated total (summer over all  $m$ ) magnetic energy in the saturated state  $\hat{\mathcal{E}}_{mag}$  and (b) torque  $G/G_{lam} - 1$  as a function of  $Re$  at  $(Lu, Rm) = (5, 20)$  (blue lines) and  $(6.78, 35)$  (green lines). Dashed lines are the power-law fits. Vertical red dotted line indicates the change in the scaling behavior of these quantities. (c) Time evolution of the volume-integrated magnetic energy of non-axisymmetric  $|m| \geq 1$  modes for  $(Lu, Rm) = (6.78, 35)$  and different  $Re = (1, 2, 3, 4, 6, 8) \times 10^4$ .

and  $Re = (1, 2, 3, 4, 6, 8) \times 10^4$ . Although for larger  $Re$  an early onset, rapid growth and saturation of the non-axisymmetric non-MRI modes happens, the saturation levels for all these modes for different  $Re$  are actually quite close to each other. However, upon taking a closer look at the saturated state [inset in Fig. 13(c)], it is seen that the magnetic energy decreases as  $Re$  increases, indicating a certain dependence on  $Re$ . In this specific example, this dependence is approximately  $Re^{-0.45}$ , which closely resembles the scaling of the magnetic energy observed for the axisymmetric MRI mode, suggesting a possible influence of the latter mode on the former.

In conclusion, the scaling laws seen in Figs. 13 and 18 for typical values of  $Lu$  and  $Rm$  in DRES-DYN-MRI experiments (Table I) certainly strengthen our finding that the bulk of the flow domain is dominated by the axisymmetric SMRI mode and validate the robustness of the scalings of the energy and torque with respect to  $Re$  and the relationship  $(\hat{\mathcal{E}}_{mag})^{-1}(G/G_{lam} - 1) \sim Re$ . Higher  $Rm \geq 35$ , at which deviation of the scaling laws has been observed at  $Re \gtrsim 2 \times 10^4$ , still represent upper limits on  $Rm$  reached when operating the DRES-DYN-TC device at full capacity and hence may not be typically used in these experiments. These scaling laws are quite useful and important since they allow us to extrapolate the characteristic quantities (energies, torques) in the saturated state to larger  $Re$  (which are numerically demanding) and thus to optimize the parameters in the DRES-DYN-MRI experiments. In this way we can minimize the effects of non-axisymmetric modes for an unambiguous detection of SMRI. However, high-resolution 3D simulations are needed to: 1. quantify the magnitude of non-axisymmetric modes for a broader  $(Lu, Rm)$ -plane and thereby 2. validate the scaling behavior of the energy and torque at lower  $Rm < 35$  but higher, experimentally relevant  $Re \gtrsim 10^6$ , which has been obtained so far at  $Re \leq 10^5$  here and in Paper II. This is outside the scope of the present paper and will be addressed elsewhere.

## V. CONCLUSION

In this sequel paper to our previous analysis of axisymmetric SMRI in a magnetized TC flow of infinitely long cylinders for DRES-DYN-MRI experiments (Papers I and II), we investigated in a similar TC flow setup the linear and nonlinear dynamics of non-axisymmetric SMRI modes. First, using linear stability analysis, we explored the parameter regime of onset of non-axisymmetric modes. Notably,  $m = 2$  mode was found to be always stable in the parameter regime of interest for  $Pm \sim 10^{-5}$  typical of liquid sodium. We show that for all  $\mu \in (0.25, 0.35]$  the dominant unstable non-axisymmetric mode has an azimuthal wavenumber  $|m| = 1$  and emerges and grow in the parameter regime achievable in the experiment, however, it always has a much smaller growth rate than that of the axisymmetric SMRI mode. In the DRES-DYN-MRI experiment, the achievable values of  $Lu$  and  $Rm$  are large enough for the onset of both axisymmetric and non-axisymmetric modes of SMRI. Hence, this study is important for determining the parameter regime over which these modes can be uniquely and unambiguously identified. We showed that for a fixed  $\mu$ , the critical  $(Lu_c, Rm_c)$  for the  $m = 0$  SMRI is several times smaller than that for the  $m = 1$  SMRI mode. This difference between the critical values of onset will allow definitive and unambiguous detection of SMRI in laboratory, which thus should be its axisymmetric mode first.

After linear analysis, we conducted nonlinear analysis of non-axisymmetric modes with azimuthal wavenumbers  $|m| \in [0, 20]$  and found that at small  $Re \lesssim 10^4$  the non-axisymmetric SMRI modes do not saturate and decay. However, at large  $Re \gtrsim 10^4$  non-axisymmetric "non-MRI" modes of hydrodynamic origin are excited in the TC flow due to turbulent boundary layer preferably near the inner cylinder wall. The turbulence in that boundary layer occurs due to the deviation of the mean azimuthal flow profile from classical TC profile as a re-

sults of the saturation of the axisymmetric SMRI mode. At large enough  $Re$ , this modified flow profile introduces steep velocity gradients at the boundaries, which becoming Rayleigh-unstable, give rise to rapid growth and saturation of non-axisymmetric "non-MRI" modes mainly concentrated in the inner boundary layer. On the other hand, the unstable non-axisymmetric SMRI modes growing initially in the original classical TC flow, decay once the flow profile is modified by the saturated axisymmetric SMRI mode. This indicates that the axisymmetric SMRI mode is essentially responsible for the growth of small-scale non-axisymmetric "non-MRI" modes within the inner boundary layer of the considered magnetized TC flow. The saturation of these modes occur at the levels few orders lower than that of the large-scale axisymmetric MRI mode, which still remains a prevalent mode in the flow.

Finally, we also explored the scaling behavior of the total magnetic energy and torque with respect to  $Re$  at several  $Lu$  and  $Rm$  in the present 3D study and compared with that of saturated axisymmetric SMRI in Paper II. We showed that the main conclusion of Paper II regarding the scaling hold true in the fully 3D case too, because of the dominant role of the axisymmetric

SMRI mode. A slight deviation from these scalings has been observed at higher  $Rm \gtrsim 35$ , due to larger amplitude of non-axisymmetric non-MRI modes, but such  $Rm$  are still somewhat higher than usual values reached in DRESDYN-MRI experiments. These scalings are quite important since they allow us to extrapolate the key characteristic quantities of the saturated state (energy, torque) to numerically demanding but experimentally relevant higher  $Re \geq 10^6$  in order to find the values of magnetic fields and velocity perturbations expected in the upcoming DRESDYN-MRI experiment.

## ACKNOWLEDGMENTS

We thank Prof. R. Hollerbach for providing the linear 1D code used in this paper and for his guidance in testing it for the present problem. We also thank Anna Guseva for providing the nonlinear code. AM acknowledges useful discussions with Vivaswat Kumar and Paolo Personnettaz. This work received funding from the European Union's Horizon 2020 research and innovation program under the ERC Advanced Grant Agreement No. 787544.

- 
- [1] E. Velikhov, Stability of an ideally conducting liquid flowing between rotating cylinders in a magnetic field, *Zh. Eksp. Teor. Fiz.* **36**, 1398 (1959).
  - [2] S. A. Balbus and J. F. Hawley, A Powerful Local Shear Instability in Weakly Magnetized Disks. I. Linear Analysis, *The Astrophysical Journal* **376**, 214 (1991).
  - [3] D. R. Sisan, N. Mujica, W. A. Tilletson, Y.-M. Huang, W. Dorland, A. B. Hassam, T. M. Antonsen, and D. P. Lathrop, Experimental Observation and Characterization of the Magnetorotational Instability, *Phys. Rev. Lett.* **93**, 114502 (2004).
  - [4] M. D. Nornberg, H. Ji, E. Schartman, A. Roach, and J. Goodman, Observation of magnetocoriolis waves in a liquid metal taylor-couette experiment, *Phys. Rev. Lett.* **104**, 074501 (2010).
  - [5] A. H. Roach, E. J. Spence, C. Gissinger, E. M. Edlund, P. Sloboda, J. Goodman, and H. Ji, Observation of a Free-Shercliff-Layer Instability in Cylindrical Geometry, *Phys. Rev. Lett.* **108**, 154502 (2012).
  - [6] D. M. H. Hung, E. G. Blackman, K. J. Caspary, E. P. Gilson, and H. Ji, Experimental confirmation of the standard magnetorotational instability mechanism with a spring-mass analogue, *Communications Physics* **2**, 7 (2019).
  - [7] Y. Wang, E. P. Gilson, F. Ebrahimi, J. Goodman, and H. Ji, Observation of Axisymmetric Standard Magnetorotational Instability in the Laboratory, *Phys. Rev. Lett.* **129**, 115001 (2022).
  - [8] G. Rüdiger, M. Gellert, R. Hollerbach, M. Schultz, and F. Stefani, Stability and instability of hydromagnetic taylor-couette flows, *Phys. Rep.* **741**, 1 (2018).
  - [9] H. Ji and J. Goodman, Taylor-Couette flow for astrophysical purposes, *Philosophical Transactions of the Royal Society of London Series A* **381**, 20220119 (2023).
  - [10] Y. Wang, E. P. Gilson, F. Ebrahimi, J. Goodman, K. J. Caspary, H. W. Winarto, and H. Ji, Identification of a non-axisymmetric mode in laboratory experiments searching for standard magnetorotational instability, *Nature Communications* **13**, 4679 (2022).
  - [11] R. Hollerbach and G. Rüdiger, New type of magnetorotational instability in cylindrical Taylor-Couette flow, *Phys. Rev. Lett.* **95**, 124501 (2005).
  - [12] R. Hollerbach, V. Teeluck, and G. Rüdiger, Nonaxisymmetric magnetorotational instabilities in cylindrical taylor-couette flow, *Phys. Rev. Lett.* **104**, 044502 (2010).
  - [13] F. Stefani, T. Gundrum, G. Gerbeth, G. Rüdiger, M. Schultz, J. Szklarski, and R. Hollerbach, Experimental Evidence for Magnetorotational Instability in a Taylor-Couette Flow under the Influence of a Helical Magnetic Field, *Phys. Rev. Lett.* **97**, 184502 (2006).
  - [14] F. Stefani, G. Gerbeth, T. Gundrum, R. Hollerbach, J. b. a. Priede, G. Rüdiger, and J. Szklarski, Helical magnetorotational instability in a Taylor-Couette flow with strongly reduced Ekman pumping, *Phys. Rev. E* **80**, 066303 (2009).
  - [15] M. Seilmayer, V. Galindo, G. Gerbeth, T. Gundrum, F. Stefani, M. Gellert, G. Rüdiger, M. Schultz, and R. Hollerbach, Experimental Evidence for Nonaxisymmetric Magnetorotational Instability in a Rotating Liquid Metal Exposed to an Azimuthal Magnetic Field, *Phys. Rev. Lett.* **113**, 024505 (2014).
  - [16] A. Mishra, G. Mamatsashvili, V. Galindo, and F. Stefani, Convective, absolute and global azimuthal magnetorotational instabilities, *Journal of Fluid Mechanics* **922**, R4 (2021).
  - [17] F. Stefani, A. Gailitis, G. Gerbeth, A. Giesecke, T. Gun-

- drum, G. Rüdiger, M. Seilmayer, and T. Vogt, The DRESHDYN project: liquid metal experiments on dynamo action and magnetorotational instability, *Geophys. Astrophys. Fluid Dyn.* **113**, 51 (2019).
- [18] A. Mishra, G. Mamatsashvili, and F. Stefani, From helical to standard magnetorotational instability: Predictions for upcoming liquid sodium experiments, *Physical Review Fluids* **7**, 064802 (2022).
- [19] M. Seilmayer, F. Stefani, T. Gundrum, T. Weier, G. Gerbeth, M. Gellert, and G. Rüdiger, Experimental Evidence for a Transient Tayler Instability in a Cylindrical Liquid-Metal Column, *Phys. Rev. Lett.* **108**, 244501 (2012).
- [20] G. Mamatsashvili, F. Stefani, R. Hollerbach, and G. Rüdiger, Two types of axisymmetric helical magnetorotational instability in rotating flows with positive shear, *Phys. Rev. Fluids* **4**, 103905 (2019).
- [21] J. F. Hawley and S. A. Balbus, A Powerful Local Shear Instability in Weakly Magnetized Disks. II. Nonlinear Evolution, *The Astrophysical Journal* **376**, 223 (1991).
- [22] E. Knobloch and K. Julien, Saturation of the magnetorotational instability, *Physics of Fluids* **17**, 094106-094106-6 (2005).
- [23] W. Liu, J. Goodman, and H. Ji, Simulations of Magnetorotational Instability in a Magnetized Couette Flow, *The Astrophysical Journal* **643**, 306 (2006).
- [24] M. Gellert, G. Rüdiger, and M. Schultz, The angular momentum transport by standard MRI in quasi-Kepler cylindrical Taylor-Couette flows, *Astronomy & Astrophysics* **541**, A124 (2012).
- [25] C. Gissinger, J. Goodman, and H. Ji, The role of boundaries in the magnetorotational instability, *Physics of Fluids* **24**, 074109 (2012).
- [26] X. Wei, H. Ji, J. Goodman, F. Ebrahimi, E. Gilson, F. Jenko, and K. Lackner, Numerical simulations of the Princeton magnetorotational instability experiment with conducting axial boundaries, *Phys. Rev. E* **94**, 063107 (2016).
- [27] D. Choi, F. Ebrahimi, K. J. Caspary, E. P. Gilson, J. Goodman, and H. Ji, Nonaxisymmetric simulations of the Princeton magnetorotational instability experiment with insulating and conducting axial boundaries, *Phys. Rev. E* **100**, 033116 (2019).
- [28] H. W. Winarto, H. Ji, J. Goodman, F. Ebrahimi, E. P. Gilson, and Y. Wang, Parameter space mapping of the Princeton magnetorotational instability experiment, *Phys. Rev. E* **102**, 023113 (2020).
- [29] O. M. Umurhan, K. Menou, and O. Regev, Weakly Nonlinear Analysis of the Magnetorotational Instability in a Model Channel Flow, *Phys. Rev. Lett.* **98**, 034501 (2007).
- [30] O. M. Umurhan, O. Regev, and K. Menou, Nonlinear saturation of the magnetorotational instability near threshold in a thin-gap Taylor-Couette setup, *Phys. Rev. E* **76**, 036310 (2007).
- [31] S. E. Clark and J. S. Oishi, The Weakly Nonlinear Magnetorotational Instability in a Local Geometry, *The Astrophysical Journal* **841**, 1 (2017).
- [32] S. E. Clark and J. S. Oishi, The Weakly Nonlinear Magnetorotational Instability in a Global, Cylindrical Taylor-Couette Flow, *The Astrophysical Journal* **841**, 2 (2017).
- [33] A. Mishra, G. Mamatsashvili, and F. Stefani, Nonlinear evolution of magnetorotational instability in a magnetized Taylor-Couette flow: scaling properties and relation to upcoming DRESHDYN-MRI experiment, *Phys. Rev. Fluids* (in press) (2023), arXiv:2211.10811.
- [34] G. I. Ogilvie and J. E. Pringle, The non-axisymmetric instability of a cylindrical shear flow containing an azimuthal magnetic field, *Monthly Notices of the Royal Astronomical Society* **279**, 152 (1996).
- [35] I. V. Khalzov, V. I. Ilgisonis, A. I. Smolyakov, and E. P. Velikhov, Magnetorotational instability in electrically driven flow of liquid metal: Spectral analysis of global modes, *Physics of Fluids* **18**, 124107 (2006).
- [36] H. Goedbloed and R. Keppens, The Super-Alfvénic Rotational Instability in Accretion Disks about Black Holes, *The Astrophysical Journal Supplements* **259**, 65 (2022).
- [37] F. Ebrahimi and M. Pharr, A Nonlocal Magneto-curvature Instability in a Differentially Rotating Disk, *The Astrophysical Journal* **936**, 145 (2022).
- [38] G. Rüdiger, M. Schultz, and D. Shalybkov, Linear magnetohydrodynamic Taylor-Couette instability for liquid sodium, *Phys. Rev. E* **67**, 046312 (2003).
- [39] D. A. Shalybkov, G. Rüdiger, and M. Schultz, Nonaxisymmetric patterns in the linear theory of MHD Taylor-Couette instability, *Astronomy and Astrophysics* **395**, 339 (2002).
- [40] R. Hollerbach and A. Fournier, End-effects in rapidly rotating cylindrical Taylor-Couette flow, in *MHD Couette Flows: Experiments and Models*, American Institute of Physics Conference Series, Vol. 733, edited by R. Rosner, G. Rüdiger, and A. Bonanno (2004) pp. 114–121.
- [41] J. Szklarski, Reduction of boundary effects in the spiral MRI experiment PROMISE, *Astron. Nachr.* **328**, 499 (2007).
- [42] Because of symmetry, the results for  $m = -1$  mode are the same as those for  $m = 1$  mode.
- [43] In the present case with resistivity, the meaning of the Alfvén resonance points is less clear though.
- [44] A. Guseva, A. P. Willis, R. Hollerbach, and M. Avila, Transition to magnetorotational turbulence in Taylor-Couette flow with imposed azimuthal magnetic field, *New Journal of Physics* **17**, 093018 (2015).
- [45] G. Mamatsashvili, F. Stefani, A. Guseva, and M. Avila, Quasi-two-dimensional nonlinear evolution of helical magnetorotational instability in a magnetized Taylor-Couette flow, *New Journal of Physics* **20**, 013012 (2018).

## Appendix

### 1. Resolution test

Figure 14 shows the azimuthal  $m$ -spectra of the magnetic energy density (see text) in the saturated state at three different azimuthal resolutions  $|m| \leq N_\phi = 10, 20, 40$  for the parameters  $Lu = 6.78$ ,  $Rm = 35$  and two different  $Re = 2 \times 10^4$  and  $Re = 4 \times 10^4$ . It can be clearly seen that these spectra converge for large  $m \geq 14$  which implies that  $N_\phi = 20$  captures significant portion of the mode energy and hence dynamics.

### 2. Magnetic energy evolution at point B of Fig. 4

Figure 15 shows the time evolution of the volume-integrated magnetic energy for  $(Lu, Rm) = (6, 30)$ , cor-

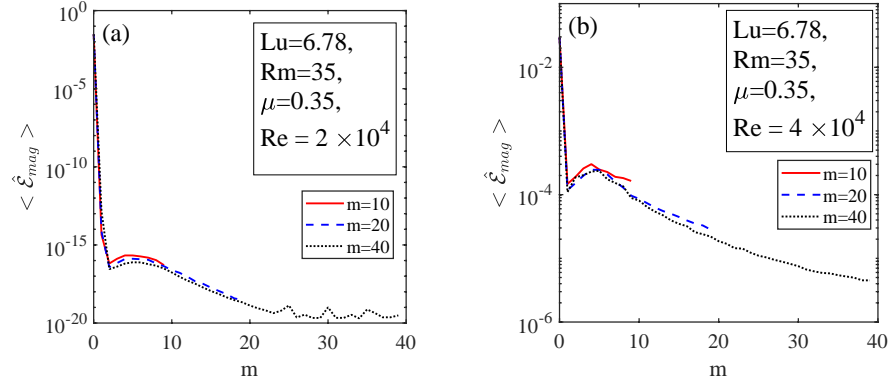


FIG. 14. Resolution test – azimuthal spectra of the magnetic energy density for different resolutions  $|m| \leq N_\phi = 10, 20, 40$  in the azimuthal  $\phi$ -direction at  $Lu = 6.78$ ,  $Rm = 35$  (point C in Fig. 4) and at two different  $Re = 2 \times 10^4$  and  $Re = 4 \times 10^4$ . The resolution  $N_\phi = 20$ , when spectra converge, appears to be enough for the analysis at these  $Re$ .

responding to point B in Fig. 4, and different  $Re = (2, 3, 4, 6) \times 10^4$ . Note that this point B is just outside but near the marginal stability curve of  $m = 1$  mode obtained for the initial TC profile. As result, the non-axisymmetric SMRI mode decays for all  $Re$  in the linear growth phase, where the flow profile is essentially TC profile. Noticeable rapid growth of non-axisymmetric modes occur at large  $Re$  (or small  $Pm$ ) as seen in panels (b), (c) and (d), which is triggered by the change in the TC flow profile as the axisymmetric SMRI mode starts to saturate. This growth is only transient and eventually decays for  $Re = 2 \times 10^4$  and  $3 \times 10^4$ , whereas saturates for  $Re = 4 \times 10^4$  and  $6 \times 10^4$ .

Figure 16 shows the time evolution of the azimuthal spectral magnetic energy density  $\mathcal{E}_{mag}(m)$  for  $m \in [0, 14]$ , the same  $(Lu, Rm) = (6, 30)$  as above and different  $Re = (3, 4, 6) \times 10^4$ . Note that for this  $Lu$  and  $Rm$  non-axisymmetric modes with smaller  $m$  decay for all  $Re$  while modes with larger  $m$  start to grow earlier before the full saturation of the axisymmetric mode, when TC has not yet been fully modified. The reason for this could be that in the middle of the exponential growth of the axisymmetric SMRI mode the boundary layers with high shear start to form and, although the shear therein may not be yet strong enough, still appears sufficient to trigger the growth of high- $m$  modes. Later, once the axisymmetric mode has reached a saturation point, a much steeper increase in the magnetic energy of all  $|m| \geq 1$  non-axisymmetric modes is seen, which is, however, not sustained for  $Re = 3 \times 10^4$ , but saturates for  $Re = 4 \times 10^4$

and  $6 \times 10^4$  at orders of magnitude higher levels.

### 3. $(r, z)$ structure of the non-axisymmetric modes in the linear regime

In Fig. 17, we plot the radial and axial velocity ( $u_r, u_z$ ) and magnetic field ( $b_r, b_z$ ) structures for all non-axisymmetric modes in the  $(r, z)$ -plane for  $Lu = 6.78$ ,  $Rm = 35$  and  $Re = 4 \times 10^4$  during the exponential growth phase [moment A in Fig. 6(c)]. It is seen from Fig. 7 that the only non-axisymmetric mode that grows is  $|m| = 1$  mode. Hence the  $(r, z)$ -structures shown here from the simulations is similar to that obtained from the linear stability analysis (see Fig. 3). Notably, the orientation of the  $(r, z)$ -structure is reversed compared to that in Fig. 3. Generally  $m = 1$  and  $m = -1$  modes have equal weights, however, the nonlinear simulation shows somewhat more preference for the  $m = -1$  mode, which could be due to initial conditions.

### 4. Scaling relations at $Rm=40$ , $Lu=8.56$

In Fig. 18, we plot the scaling behavior for the saturated magnetic energy  $\hat{\mathcal{E}}_{mag}$  and torque  $G/G_{lam} - 1$  as a function of  $Re$  for  $Lu = 8.56$  and  $Rm = 40$ . Similar to the observation in Figs. 13(a) and 13(b), the scaling of  $\hat{\mathcal{E}}_{mag}$  and  $G/G_{lam} - 1$  changes after  $Re > 2 \times 10^4$  due to stronger non-axisymmetric non-MRI modes. However, the scaling relation  $(\hat{\mathcal{E}}_{mag})^{-1}(G/G_{lam} - 1) \sim Re$  is still satisfied.



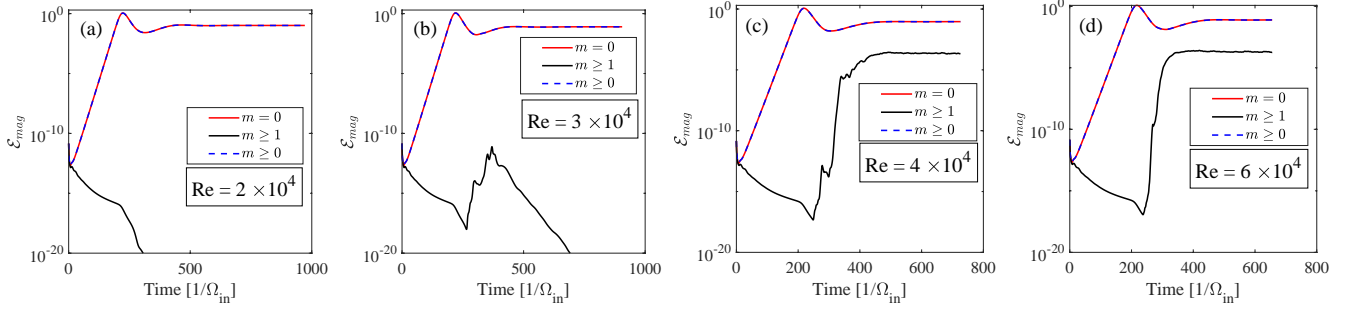


FIG. 15. Time-evolution of the volume-integrated magnetic energy  $\mathcal{E}_{mag}$  for the total ( $m \geq 0$ ), axisymmetric ( $m = 0$ ) and non-axisymmetric ( $|m| \geq 1$ ) modes at  $(Lu, Rm) = (6, 30)$  (point B in Fig. 4) at different  $Re = 2 \times 10^4$  (a),  $3 \times 10^4$  (b),  $4 \times 10^4$  (c) and  $6 \times 10^4$  (d).

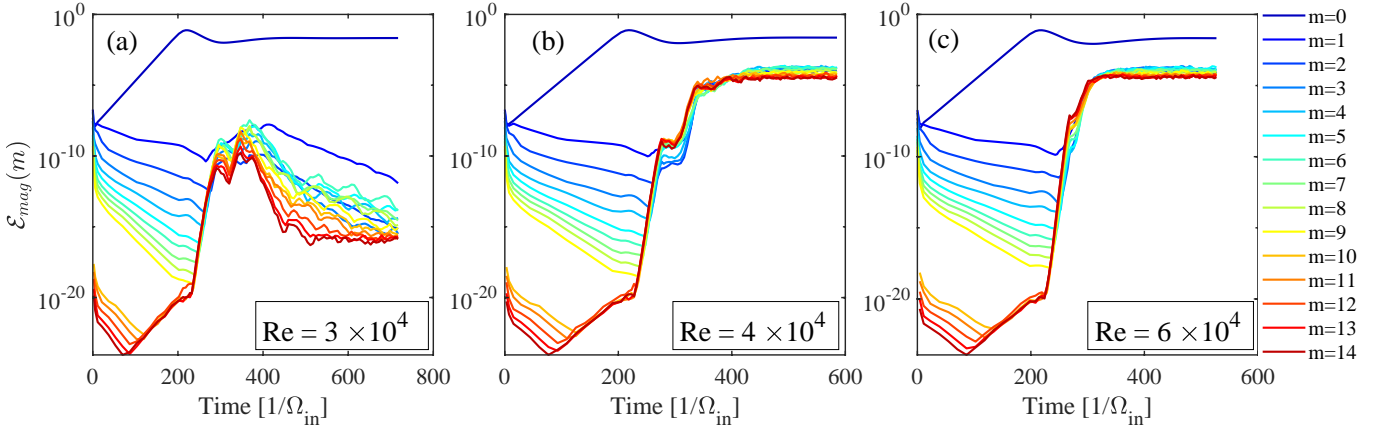


FIG. 16. Time evolution of the azimuthal spectral magnetic energy density  $\mathcal{E}_{mag}(m)$  of each  $m \in [0, 14]$  for  $(Lu, Rm) = (6, 30)$  and different  $Re = 3 \times 10^4$  (a),  $4 \times 10^4$  (b) and  $6 \times 10^4$  (c).

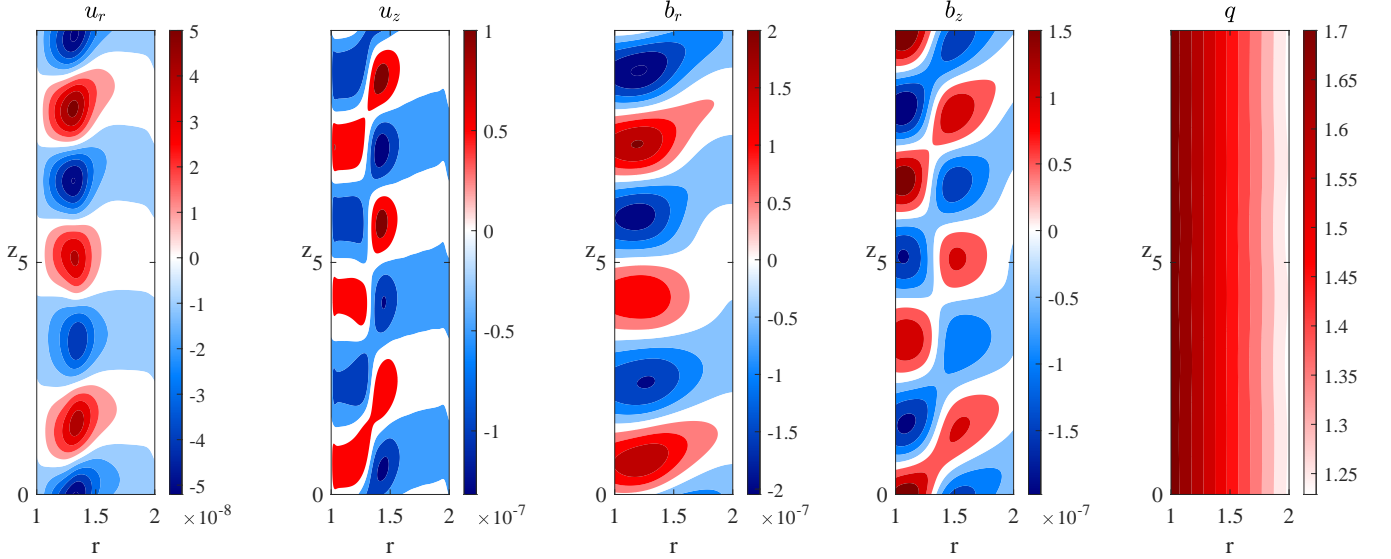


FIG. 17. Radial and axial velocity ( $u_r, u_z$ ) and magnetic ( $b_r, b_z$ ) field structures of the non-axisymmetric modes in the  $(r, z)$ -plane during the exponential growth stage [moment A in Fig. 6(c)], which are essentially dominated by  $|m| = 1$  component, for  $(Lu, Rm) = (6.78, 35)$  and  $Re = 4 \times 10^4$ .

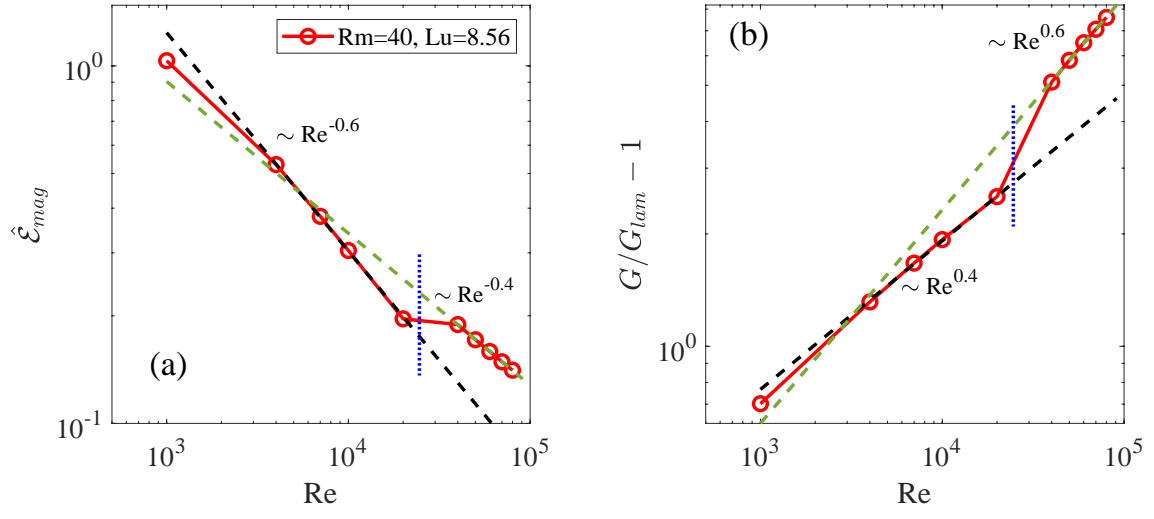


FIG. 18. Same as Figs. 13(a) and 13(b) but for  $Lu = 8.56$  and  $Rm = 40$ . Blue dotted line shows the change in the scaling behavior for the saturated magnetic energy  $\hat{\mathcal{E}}_{mag}$  and torque  $G/G_{lam} - 1$  due to stronger non-axisymmetric non-MRI modes.